Gravity-driven sliding and associated deformations along complex submarine slopes: a laboratory modeling approach based on constraints observed offshore Martinique Island (Lesser Antilles)

Morgane Brunet, Thierry Nalpas, Erwan Hallot, Anne Le Friant, Georges Boudon, Jean-Jacques Kermarrec

BSGF - Earth Sciences Bulletin 2023, 194, 12
© M. Brunet *et al.*, Published by EDP Sciences 2023
https://doi.org/10.1051/bsgf/2023008

BSGF
Earth Sciences Bulletin
Available online at:
www.bsgf.fr

Gravity-driven sliding and associated deformations along complex submarine slopes: a laboratory modeling approach based on constraints observed offshore Martinique Island (Lesser Antilles)

Morgane Brunet[1,2,*], Thierry Nalpas[1], Erwan Hallot[1], Anne Le Friant[3], Georges Boudon[3] and Jean-Jacques Kermarrec[1]

[1] Université de Rennes, CNRS, Géosciences Rennes – UMR 6118, 35000 Rennes, France
[2] Géosciences Rennes, Université de Rennes 1, Campus Beaulieu, 35042 Rennes, France
[3] Université de Paris, Institut de physique du globe de Paris, CNRS, 75005 Paris, France

Received: 27 July 2022 / Accepted: 6 June 2023 / Publishing online: 10 August 2023

Abstract – Submarine gravity-driven sliding of sediments are common processes in the vicinity of volcanic islands. In the Lesser Antilles arc, the Montagne Pelée volcano on Martinique Island underwent several flank-collapse events during its long-term eruptive history, resulting in debris avalanches. When the debris avalanches entered into the seawater, they were emplaced over the unstable slope of the volcano, triggering a seafloor sediment failure and massive landslides downslope. Using a laboratory modeling approach, we simulated the gravity-driven sliding of a sand layer lying above a silicone layer. The experiments were performed using various slope geometries (slope lengths and number of slope breaks separating the slopes with different angles), under both dry and aqueous conditions, and while varying the amount of additional sand inputs upslope. The resulting deformations were characterized in each experiment in order to compare the obtained structures with those shown by the seismic lines offshore to the west of Martinique Island. During all the experiments, a compressional frontal deformation zone made of several reverse faults formed downslope, often near the slope breaks. Downslope, a portion of the sediments was mostly displaced and poorly deformed in a damping zone, while an extensional deformation zone formed upslope. The displacements of the surficial markers were measured through time to characterize the sliding dynamics. Our study demonstrates that the slope geometry and additional sand inputs primarily favor and increase the sliding deformation, whereas the hydrostatic pressure plays a secondary catalytic role over time. These results provide new constraints on the driving factors and their consequences on gravity-driven sliding in terms of deformations and runout distance over time. This may have a significant impact on the associated hazard assessment related to offshore infrastructures, in a region known for its seismic and volcanic risks.

Keywords: laboratory experiments / submarine slope / gravity-driven sliding / morphological front / slope geometry / hydrostatic pressure

Résumé – Glissements gravitaires et déformations associées le long de pentes sous-marines complexes : approche expérimentale basée sur les contraintes observées au large de la Martinique (Petites Antilles). Les glissements gravitaires sous-marins d'origine sédimentaire sont fréquents aux abords des îles volcaniques. Dans les Petites Antilles, le volcan de la Montagne Pelée en Martinique a subi plusieurs épisodes d'effondrements des flancs au cours de son histoire éruptive, donnant lieu à des avalanches de débris. Lorsque ces avalanches de débris entrent en mer, elles se déposent sur la pente sous-marine instable du volcan, déclenchant une déstabilisation des sédiments en mer et d'importants glissements qui se propagent sur les fonds marins. A partir d'expériences en laboratoire, nous avons modélisé le processus de glissement gravitaire d'une couche de sable sur une couche de silicone. Les expériences ont été réalisées en utilisant différentes géométries de pente (longueurs, angles et nombre de rupture de pente), à sec et sous l'eau, puis en variant les quantités de sable ajoutées en haut de pente. Les déformations observées ont été caractérisées à chaque expérience afin de comparer les structures obtenues avec celles identifiées sur les

*Corresponding author: morgane.brunet@univ-rennes1.fr

lignes sismiques au large de la côte ouest de la Martinique. Durant toutes les expériences, un front de déformation compressif constitué des plusieurs failles inverses se formait en bas de pente, le plus souvent près des ruptures de pentes. Le bas de pente est généralement caractérisé par un déplacement simple des sédiments, très peu déformés, constituant une zone d'accommodation de la déformation, alors qu'une zone en extension se forme systématiquement en haut de pente. Le déplacement des marqueurs à la surface des modèles a été mesuré au cours du temps afin de caractériser la dynamique de glissement. Nos travaux montrent que la géométrie de pente et les apports de sable favorisent le glissement et augmente la déformation, alors que la pression hydrostatique semble jouer un rôle secondaire de catalyseur au cours du temps. Ces résultats apportent de nouvelles contraintes sur les facteurs moteurs et leurs conséquences sur les glissements gravitaires en termes de déformations et de distance de propagation au cours du temps. Ces observations ont des implications importantes pour l'évaluation des risques associés aux infrastructures sous-marines, notamment dans une région soumise aux aléas sismiques et volcaniques.

Mots clés : expériences en laboratoire / pente sous-marine / glissement gravitaire / front morphologique / géométrie de pente / pression hydrostatique

1 Introduction

Since the 1960s, numerous field studies have described gravity-driven sliding processes occurring in sedimentary basins and continental margins (Wise, 1963; Cloos, 1968), as well as in mountain ranges, where sliding results in the formation of thrust faults (Hudlestone, 1976, 1977, 1980; Talbot, 1979, 1981; Kligfield, 1979; Graham, 1981; Merle, 1982). Siddans (1984) has suggested that the moving direction of these thrusts is determined by the surface and basal slopes of the affected sedimentary piles. Burollet (1975), Brun and Choukroune (1983) and Vendeville (1987) were among the first authors to propose that the deformation within passive margins results from gravity-driven sliding that propagates above décollement layers.

Considerable attention has been placed on deformation induced by gravity in sedimentary basins over the past several decades. Based on experimental patterns, Rettger (1935) demonstrated that local sedimentary input into a system may trigger a gravity-driven deformation within the underlying layers. Since this work, other studies have shown that a sedimentary pile may slide and spread, even down low slopes, under the effect of its own weight. These displacements can be accommodated either through translational motions (*i.e.*, pure slide) when the basal décollement layer is submitted to an elevated pore pressure (Hubbert and Rubey, 1959; Hsü and Siegenthaler, 1969; Merle, 1982), or through rotational motions (*i.e.*, slump) when the basal layer is made up of low-strength lithologies (*i.e.*, shales, clays, evaporites; Kehle, 1970; Fletcher and Gay, 1971; Price, 1977; Ramberg, 1977; Déramond, 1979).

Today, it is well-recognized that the deformation induced by gravity in sedimentary basins is characterized by sub horizontal basal décollement layers as well as both extensional and compressional deformation patterns that develop upslope to downslope respectively (Crans *et al.*, 1980; Letouzey *et al.*, 1995). Typical normal faults, horsts and grabens form upslope, regardless of the lithologies within the layers, the density, viscosity and thickness ratios, or extensional velocity values (Vendeville and Jackson, 1992). Meanwhile, fold and thrust systems develop downslope. The intensity of the extensional and compressional deformations also appears to be conditional upon the sediment inputs within the whole system. When the sedimentary inputs stop, the sliding layer and the internal deformation progressively cease.

Many studies have investigated the mechanisms triggering the gravity-driven sliding of an unstable sediment layer along a slope. Nowadays, it is acknowledged that the driving load for sliding increases as sedimentary inputs preserved upslope cause the layer to progressively thicken. Sliding starts once the resistance downslope (*i.e.*, the thickness) cannot support the driving charge upslope any longer. These processes have been largely analyzed through a large number of field examples (*e.g.*, in the Niger Delta: Doust and Omatsola, 1990; Cohen and McClay, 1996; Haack *et al.*, 2000; Corredor *et al.*, 2005; Cobbold *et al.*, 2009; Rouby *et al.*, 2011), analogue modeling experiments (Cobbold and Szatmari, 1991; Koyi, 1996; Szatmari *et al.*, 1996; Ge *et al.*, 1997; McClay *et al.*, 1998, 2003; Gaullier and Vendeville, 2005; Vendeville, 2005; Mourgues *et al.*, 2009) and numerical simulations (*e.g.*, Cohen and Hardy, 1996; Gemmer *et al.*, 2004, 2005; Albertz *et al.*, 2010; Ings and Beaumont, 2010). The role of fluid overpressures at the base of sedimentary layers during compression has also been highlighted (Cobbold *et al.*, 2009).

The main characteristics of the observed submarine landslide occurring offshore Martinique Island (Lesser Antilles arc, Fig. 1) (Le Friant *et al.*, 2015; Brunet *et al.*, 2016) have been used to constrain the experimental device used in the present study and some of the experiments. As usual, for analogue modeling studies, the approach required simplifying the complexity of the natural system by respecting, in the laboratory, the scaling laws for the geometry, kinematics and dynamics of the processes (Hubbert, 1937; Ramberg, 1981). Despite these simplifications, and over a period of time lasting up to several hours and at a manageable size, the experiments conveniently reproduce long and slow natural processes (so slow that they may appear to be frozen at the scale of a human's lifetime) involving objects of huge sizes. These experiments can be used to (i) test different settings and physical parameters and (ii) better understand the influence of each individual parameter on the behavior of the whole system. Therefore, the results of the present study apply beyond the geological context of the Montagne Pelée and its offshore submarine flank. Other volcanoes from the Lesser Antilles, other insular arcs, as well as intraplate volcanic islands, are concerned by flank collapses and submarine landslides. It is thought that these results apply in any geological context that involves slides of poorly consolidated sediments just above complex submarine, lacustrine, or aerial slopes.

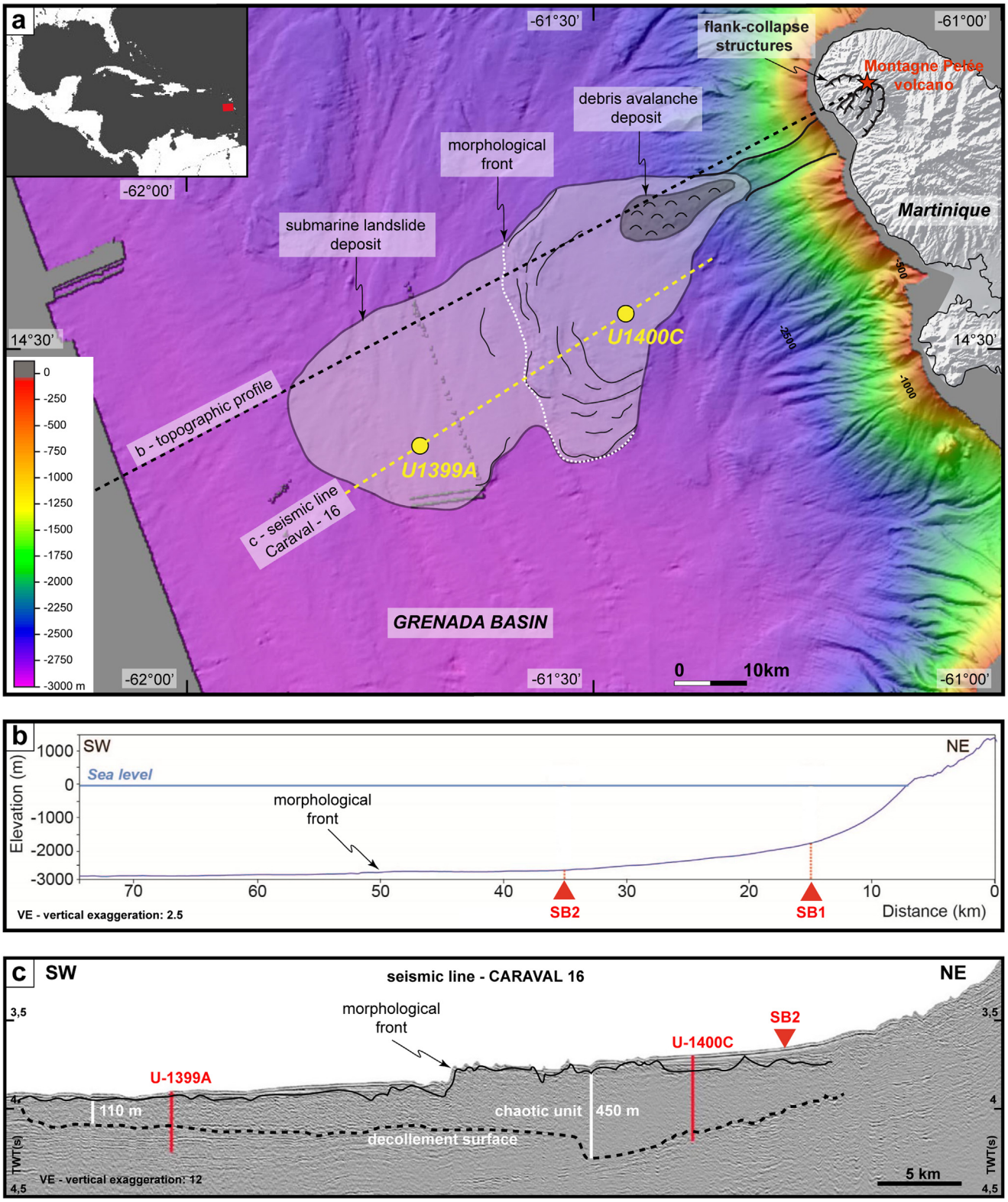

Fig. 1. Location, extent of the mass wasting deposits associated with the flank collapses from the Montagne Pelée volcano (Martinique Island) and corresponding profiles. (a) Interpreted bathymetric map of the mass wasting deposit showing the locations of the IODP Expedition 340 drill sites (U-1399A & U-1400C) and topographic profiles (b) and seismic line (c). (b) Topographic profile. SB: slope break. (c) CARAVAL 16 seismic line. Black lines: interpretative limits of the landslide unit deposit (dashed line: basal décollement layer). Terrestrial digital elevation model from the Institut National Géographique et Forestière; Marine geophysical data from the oceanographic cruises AGUADOMAR (1999); CARAVAL (2002) and GWADASEIS (2009) (Deplus *et al.*, 2001, 2002; Feuillet *et al.*, 2010).

Table 1. Scaling parameters of the experiments.

Scaling parameters	L (m)	t (s)	V (m/s)	ρ (kg/m^3)	g (m s^{-2})	σ (Pa)
Nature (N)	1000	1×10^{10}	4×10^{-7}	2000	9.8	2×10^{7}
Experiment (E)	0.01	2.7×10^{4}	1.5×10^{-6}	1500	9.8	1.5×10^{2}
Ratio N/E	1×10^{5}	3.7×10^{5}	0.27	1.3	1	1.3×10^{5}

L: lengths; t: time; V: velocity; ρ: density; g: gravity acceleration; σ: stress; t = 7.5 h in the experiments represent around 300 years in nature; v = 0.5 cm/h in the experiments represent around 0.14 cm/h in nature. The ratios Nature/Experiment (N/E) for L, t and σ are of the same orders of magnitude.

Several studies have used analogue modeling to investigate the evolution of volcanic edifices, and the associated mass-movement processes such as the spreading of volcanoes and debris avalanches resulting from flank-collapse events (Merle and Borgia, 1996; Walter and Troll, 2003; Walter and Amelung, 2006; Oehler *et al.*, 2005; Delcamp *et al.*, 2008, 2012; Byrne *et al.*, 2013; Kervyn *et al.*, 2014). However, to the best of our knowledge, no studies have investigated the offshore consequences of these onshore instability processes, such as the development of large-scale submarine landslides (Watt *et al.*, 2012a, b, 2021; Brunet *et al.*, 2016). Based on our present level of knowledge so far, no analogue modeling studies have investigated submarine landslides triggered by volcano flank-collapse events and their consequences on the deformation of marine sediments. In this framework, this study investigates the mechanisms that govern the submarine landslide propagation induced by massive and sudden sedimentary input (*i.e.*, debris avalanche) over simple and complex submarine slopes.

2 Geological context

The Lesser Antilles volcanic arc results from the subduction of the Atlantic plate beneath the Caribbean oceanic plate since approximately 40 Ma ago (Martin-Kaye, 1969; Wadge, 1984; Bouysse *et al.*, 1990; DeMets *et al.*, 2000). Along the active arc, several volcanoes experienced collapsed flanks during their evolution, resulting in mass wasting deposits mostly within the Grenada Basin located to the west of the arc (*e.g.*, Boudon *et al.*, 2007; Le Friant *et al.*, 2009; Lebas *et al.*, 2011; Watt *et al.*, 2012a, b; Crutchley *et al.*, 2013; Trofimovs *et al.*, 2013; Cassidy *et al.*, 2014).

The Montagne Pelée volcano on Martinique Island (Fig. 1a) is one of these. It has been active since roughly 130 ka and underwent three major flank-collapse events affecting the western flank of the volcano (Deplus *et al.*, 2001; Le Friant *et al.*, 2003a, b; Boudon *et al.*, 2005, 2007; Germa *et al.*, 2011). In 2012, during the IODP Expedition 340, the submarine landslide deposits were drilled and as a result, the mass wasting processes that were involved were reinterpreted (Le Friant *et al.*, 2015; Brunet *et al.*, 2016). The submarine mass wasting deposit is 50 km long and 40 km wide and covers an area of 2100 km^2 (Fig. 1a). First interpreted as debris avalanche deposits (Le Friant *et al.*, 2003a), it was determined that it mostly corresponded to submarine landslide deposits, except upslope where debris avalanche deposits were clearly identified (Fig. 1a). As a result, Brunet *et al.* (2016) proposed a new depositional model linking onshore processes (*i.e.*, Montagne Pelée flank-collapse events and associated debris avalanches) with submarine instability processes in Martinique. The authors suggest that the first flank-collapse event produced a large debris avalanche flowing down to the Grenada Basin, which weakened and then initiated seafloor-sediment failure, triggering a major submarine landslide downslope. Then, the second and third debris avalanche deposits remobilized the unconsolidated surficial sediments within the proximal part of the submarine landslide deposit.

However, several questions remain and motivate this study: is it possible that a sudden sedimentary input could trigger a submarine landslide? Could a regular input trigger one? If so, in which conditions and how does it propagate? If not, is there some other possible initiating factor? Does the slope's geometry – and especially slope break occurrences – influence landsliding? To what extent?

Using numerical simulations, Brunet *et al.* (2017) demonstrated that debris avalanches are slowed down when flowing over a slope break, suggesting that debris avalanche deposits have a limited lateral extent, as shown off Martinique Island (Fig. 1a). Based on bathymetric data, the slope geometry offshore the island shows two slope breaks (SB1 & SB2, Fig. 1b). From the volcano summit to the landslide's toe, the main slope is: (i) 15° to 10° in the continuity of the aerial volcano flank, (ii) 5° to 2° beyond a first slope break (SB1, located approximately 7.5 km away from the coastline), and (iii) < 2° beyond a second slope break (SB2, approximately 30 km away from the coastline). Seismic reflection and drilling data were used to constrain the submarine landslide morphology, which is characterized by a chaotic unit showing a morphological front at the surface and a seismic reflector interpreted as a décollement layer at the base (Fig. 1c). The landslide thickness reaches a maximum of 450 m in the axial part but can be 110 m in both the distal and lateral parts (Fig. 1c). The estimated volume is roughly 300 km^3. Based on the flank collapse structures on land, the estimations of the debris avalanche material uprooted from the volcano during the flank-collapse events vary from 16.7 km^3 up to 40 km^3 (Le Friant *et al.*, 2003a; Germa *et al.*, 2015). Therefore, this cumulated debris avalanche volume represents only approximately 13% of the total slide volume.

Cores from the IODP Expedition 340 were drilled within both the central and distal parts of the submarine landslide deposit (see Figs. 1a and 1c for the location). Hemipelagic sediments dominate in the slide unit in both cores. They alternate with volcanoclastic turbidites, which may form layers up to 10 m thick, with interspersed debrites (*i.e.*, debris flow deposits) and tephra layers of variable thicknesses. These lithologic alternations result in a multi-layered structure with

Table 2. Main initial experimental conditions.

Experiment	SB(s)	P1-α (deg)	P2-α (deg)	P3-α (deg)	P1-L (cm)	P2-L (cm)	P3-L (cm)	CM (g)	SI (type)
GD10 GA10	1	12	–	2	15	–	40	–	–
GD11 GA11	1	12	–	2	35	–	40	–	–
GD12 GA12	2	12	2	0.5	15	20	40	–	–
GD07 GA07	2	12	4	2	15	20	40	–	–
GD18 GA18	2	12	2	0.5	15	20	40	150	Initial
GD15 GA15	2	12	2	0.5	15	20	40	450	Periodic
GD14 GA14	2	12	2	0.5	15	20	40	450	Initial

SB: number of slope breaks; P1, P2 and P3: angle values and lengths of the slopes, respectively; CM (where appropriate): cumulated mass of sand added during the experiments with SI (sediment input).

many contacts that may have acted as décollement layers in the system. In addition, the cores revealed that the relative proportion of clay minerals, likely resulting from the alteration of former ash tephra, is larger in the vicinity of the island than in the Grenada Basin (80% *vs.* 40%, respectively) and may have contributed to the landslide process (Brunet *et al.*, 2016).

3 Scaling and analogue materials

Our goal is to model the sliding of a layer of known thickness along slopes, for which the angle values may vary downslope. The geometrical scaling of the experiments was defined from the example illustrated in Figure 1. An experimental length scale ratio (L0) of 1 cm for 1 km in nature has been chosen (Tab. 1). The slope values and their layouts in the experiments were also calibrated to be representative of the natural example (Tab. 2). In nature, the heterogeneous lithological composition of the submarine landslide and its basal décollement layer are documented by the deep drilling cores from the IODP Expedition 340. First, the landslide is mainly composed of volcanic sandy turbidites (Le Friant *et al.*, 2013, 2015; Brunet *et al.*, 2016), which gives a fragile rheological behavior to the landslide layer, which is commonly modelled by using sand material (Faugère and Brun, 1984; Nalpas *et al.*, 1999; Barrier *et al.*, 2013). The basal décollement layer is characterized by intercalated tephra layers in hemipelagic sediments sequences. The strength contrast between both lithologies induces low shear strength levels acting as preferential weak layers for sliding under significant constraints. This low strength behavior of the basal surfaces is widely modeled in the literature using a ductile material such as silicon putty (Vendeville *et al.*, 1987; Cobbold *et al.*, 1989; Mauduit *et al.*, 1997; Mourgues *et al.*, 2009). Therefore, the heterogeneous nature of both the landslide and basal décollement layer had to be simplified using a two-layer system made of silicone putty and sand.

The modelling techniques used are similar to those usually used for experiments dealing with brittle-ductile systems in the Laboratory of Experimental Tectonics of Geosciences Rennes (Rennes University, France) and which have been described in numerous studies (*e.g.*, Faugère and Brun, 1984; Vendeville *et al.*, 1987; Davy and Cobbold, 1991; Cobbold and Castro, 1999, 2009). Dry Fontainebleau quartz sand (SIBELCO NE34) with Mohr–Coulomb properties was used to model the brittle (*i.e.*, frictional) behavior of the sedimentary rocks. It exhibits a mean grain size of approximately 250 μm, an internal friction angle within the range of 30°–35°, negligible cohesion, and an average density close to 1.5 (Tab. 1; Krantz, 1991; Klinkmüller *et al.*, 2016). The silicone putty (uncolored SGM 36 manufactured by Rhône-Poulenc, France) is used to model the ductile (*i.e.*, viscous) behavior of weak sedimentary rocks. It was chosen because of its density of 0.96 and an almost Newtonian viscosity of about 10^4 Pa·s under low stresses, at room temperature. As the natural detachment layer is not viscous, the basal silicone layer only represents a technical expedient to enhance sliding that cannot be correctly scaled to nature. Regardless, models provide valuable information regarding the deformation style. In most of the experiments, the sliding brittle layer mostly consists of a 5.10^{-3} m-thick sand layer corresponding to poorly consolidated sediments in nature that deform in a brittle manner under sufficient stress. It overlies a 2.10^{-3} m-thick silicone putty layer simulating a basal décollement layer that allows sliding to occur.

The sedimentary input (*i.e.*, debris avalanche) was represented by dry Fontainebleau sand and therefore, during some of the experiments, the thickness of the sliding layer varied from 5.10^{-3} m up to about 10^{-2} m in order to simulate punctual and periodical debris avalanches.

4 Experimental set-up and protocols

The geometric characteristics (thickness and length of the deposit, slope, sediment inputs, etc.) of the experimental device have been set-up using the interpreted marine geophysical data (Brunet *et al.*, 2016) acquired offshore

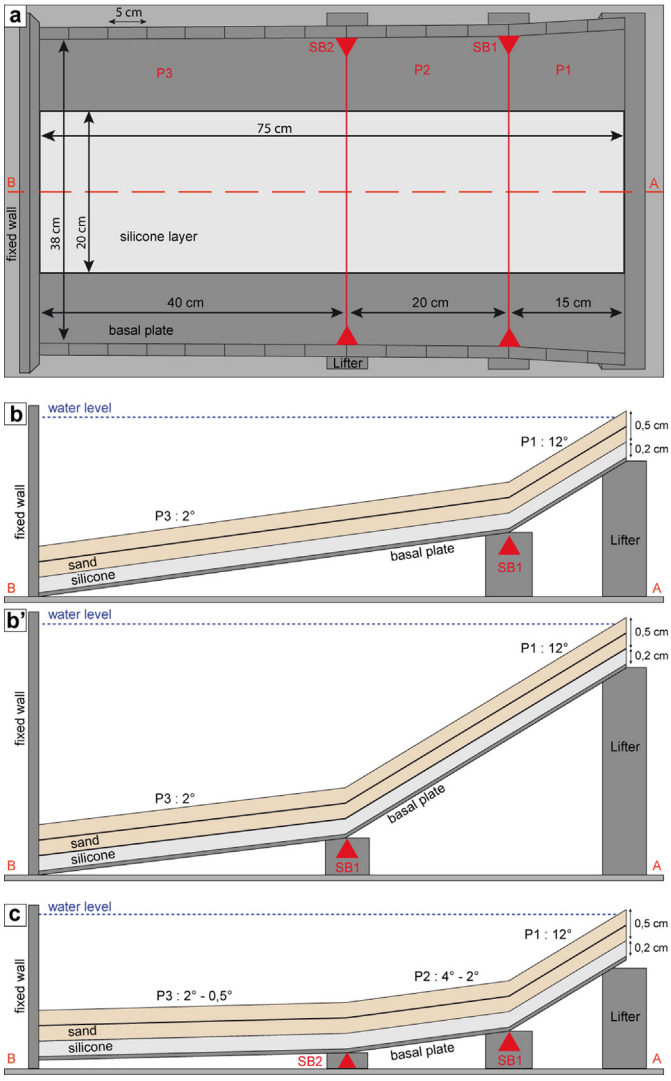

Fig. 2. Schematic illustrations of the experimental devices. (a) Surface view for the experiment with two slope breaks (solid red lines) and involving three plates (P1, P2 & P3); the dashed red line shows the location of the axial cross-sections. (b,b') Cross-section views of the device for the experiments with one slope break (two plates of different lengths, P1 & P3). (c) Cross-section views for the experiments with two slope breaks (see (a)). (b,c) The vertical exaggeration is x8. The red triangles show the location of the slope breaks (SB1 and SB2).

Martinique (Deplus *et al.*, 2001, 2002; Le Friant *et al.*, 2003a; Fig. 1). Although the area and volume of the slide models are proportional to the real ones, it is important to note that the slide area – and indirectly the volume – are limited by the dimensions of the underlying silicone layer (Figs. 2 and 3). The modeled slide propagation distance is proportionally shorter than the natural one (50 cm in the model, which is equal to 25 km in nature instead of 50 km), but still is within the same order of magnitude. Only the thickness "deposit" may be one order of magnitude higher compared to the real deposit.

In addition, the study aims to investigate the gravity-driven sliding dynamics and deformation propagation over submarine slopes. Each experiment was systematically carried out in dry and underwater conditions, in order to get first-order observations on the potential influence of hydrostatic pressure on sliding.

In total, 20 experiments were carried out (Brunet, 2015); six of them were set-up to work out the experimental device and protocols (not presented in this study). Among the 14 other experiments presented herein, constant parameters were applied (silicone and sand two-layer sizes; the upslope slope-angle value was fixed at 12°, Tab. 2). Some other parameters varied from one experiment to another (number, lengths and angle values of the downslope plate or plates; planed, additional sand input or inputs; dry or aqueous conditions; Tab. 2).

Wall edges measuring 1 cm-high laterally limit the experimental device, which is 75 cm-long and 42 cm-wide, and an additional fixed wall is located downslope (Fig. 2a). The experimental device is composed of rigid basal plates set up at different angle values from the horizontal (Figs. 2b, 2b' and 2c). For all the experiments, from upslope to downslope, the angle values decrease. Two types of experiments were performed: two plate experiments exhibit a single slope break (labelled SB1 between plates P1 and P3), whereas three plate experiments exhibit two-slopes breaks (labelled SB1 and SB2 between plates P1 and P2, and P2 and P3, respectively; see Tab. 2 for the angle values for each experiment).

Before each experiment, a 0.2 cm-thick and 20 cm-wide silicone putty basal layer was set in the middle of the plates, all along the slopes (Fig. 2). Then the whole surface of the plates, including the silicone putty layer, was covered with sand to reach a total thickness of approximately 0.7 ± 0.2 cm. Thus, only the axial part of the experimental device was covered by the silicone plus sand two-layer. This configuration was chosen in order to minimize potential rigid sidewall effects. Above the silicone, the sand layer was comprised of white sand with an intercalated black sand marker (Figs. 2b, b' and c) so as to be able to analyze the internal deformation at the end of the experiment *via* the cross-section views. Black sand was also sprinkled on top of the sand layer, and white sand was used to draw parallel markers on the sand surface to visualize the displacement (*e.g.*, Figs. 3a and 3c). The colored sand had the same physical properties as the white sand.

The three slope models involving additional sand inputs, upslope (over the P1 zone), during the course of the experiments, were constrained to redesign the surficial white makers after each new sand supply. The inputs were set either only once at the start of the experiment (a single sand input of 150 or 450 g) or periodically by adding 75 g of sand every 12 h so as to accumulate six sand inputs (450 g in total) for the whole duration of the experiment (Tab. 2). The quantity of added sand was scaled from estimations of the cumulated debris avalanche volumes generated by the Montagne Pelée volcano (*i.e.*, 40 km^3), compared to the submarine slide mass volume (300 km^3), representing 13%, with 450 g of sand corresponding to the total volume of debris avalanche deposits. We ran three experimental scenarios: the first scenario, with an initial input of 150 g of sand (G18), and a second scenario, with an initial input of 450 g of sand, were tested to represent the deposition of the three cumulated debris avalanche deposits. The third scenario tested multiple deposition events. The preliminary tests showed that the sliding was not moving anymore after 84 h of the experiment. Next, we decided to

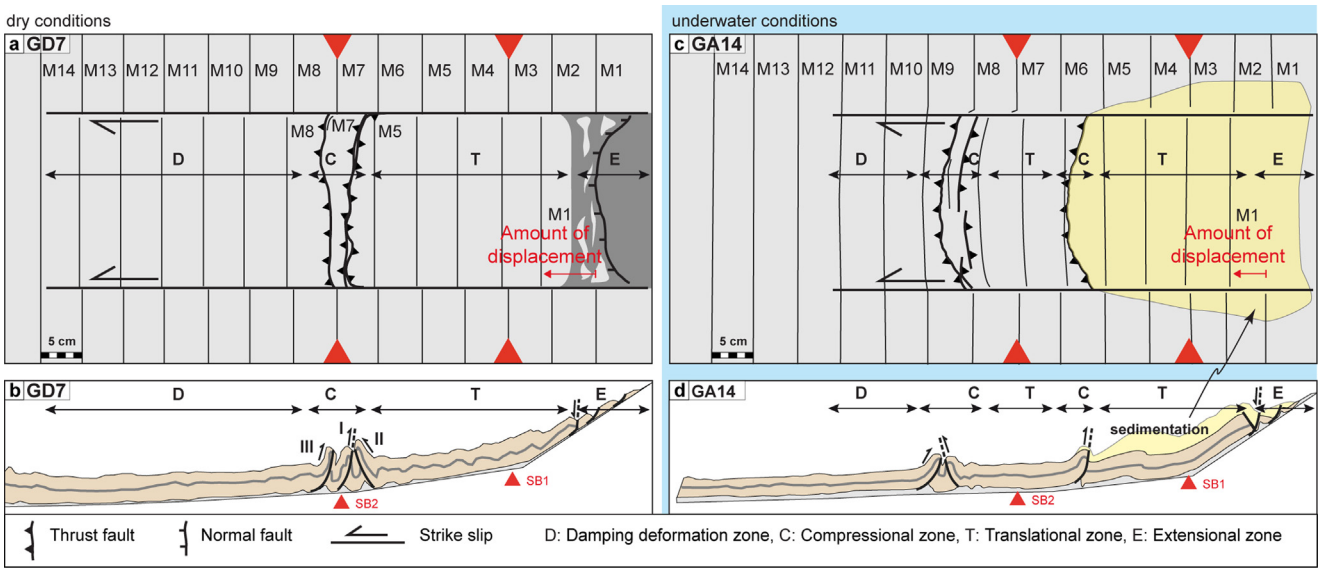

Fig. 3. Examples of the final results obtained in the models. (a,b) Dry experiment GD7 without additional sand input. (c,d) Aqueous experiment GA 14 with additional sand input. Interpretative drawings of (a,c) the final surface views and (b,d) the cross-sections. E, T, C and D denote the deformation zones in the surface view (E: extension, T: translation, C: compression, D: damage); the final displacement of marker M1 is also highlighted. I, II and III indicate the order in which the faults spear on the cross-section. The vertical exaggeration in the cross-sections is x4.4.

distribute the sand input (450 g) periodically throughout this time frame (84 h), which was equal to 75 g of sand every 12 h, representing six inputs during the G15 experiment.

All other conditions being equal, each model was carried out once in a dry condition and once under water (aqueous condition). For the dry conditions, the experimental device was left in the open ambient air. For the aqueous conditions, the device was installed in a tank (110 × 70 × 40 cm) filled with water to cap the sand layer upslope. Therefore, the experiments are labelled GAX or GDX: X refers to the experiment number, and A or D indicates either Aqueous or Dry conditions, respectively. From upslope to downslope, the slope breaks (where appropriate) and the surficial markers were labelled SB1, SB2 and M1, M2, M3, ..., M14, respectively (Fig. 3).

A NIKON D90 camera with an AF-S DK NIKKOR 18–55 mm f/3.5–5.6G VR lens and light spots suspended above the model were used to take pictures of the model surface at regular time intervals (15 min). This was done to follow the evolution of the sliding during each experiment.

In practice, each run lasted 84 h, *i.e.*, three and a half days. The length of the runs was determined according to the preliminary experiments showing that beyond that amount of time, for some experiments, the displacements became almost indiscernible and were < 1 mm during the last 12 h. Then, the water was removed from the tank (aqueous conditions only), and the models were entirely covered with new sand that was sprinkled on top along with water (dry conditions) in order to preserve the structures by making serial cross-sections parallel to the slope (direction of the sliding) of the models.

5 Experimental results

Photographs were used to measure the displacements of each surficial marker with time for each experiment, with an uncertainty of ± 1 mm (Fig. 3). These data were used to estimate the displacement velocities. The final displacement of the first marker (M1) was used to estimate the total shortening across each model (Tab. 3). The last photographs taken (surface and cross-section) were used to determine the distribution of the observed successive, surficial deformation zones and their lengths from upslope to downslope (Tab. 3). They also localize the final position of the observed morphological front given by the axial distance from the top of the upslope plate to the farthest downslope topographic positive anomalies encountered in the compressional zone: C. This distance is referred to as the morphological front distance (Fig. 3 and Tab. 3). The final spatial organization and the characteristics of the faults that developed close to the morphological front for each experiment were analyzed using each axial cross-section (located at the center of the model).

Tables 2 and 3 provide the experimental conditions and the main results for the experiments, respectively. All the experiments underwent spontaneous sliding and deformation of the silicone-sand layer. Given the experimental set-up, sliding is located in-between two strike-slip faults (Fig. 3a) that initiated as soon as the experiments were set up and which developed along the margins of the axial silicone layer. Simultaneously, normal faults formed upslope and fold and thrust systems developed downslope. The most downslope of these systems is referred to as the morphological front. The cross-sections reveal that the morphological fronts were made of several reverse faults, which are said to be synthetic when verging downslope and antithetic when verging upslope (Fig. 4a). During an experiment, the reverse faults may have successively formed as a sequence from upslope to downslope (Fig. 4b) or may be out of sequence when a newly formed fault developed upslope relative to an earlier one (Fig. 4c).

Irrespective of the experimental conditions, a typical distribution of the deformation zones developed. It shows, successively, from upslope to downslope: (1) an extensional

Table 3. Summary of the results for the experiments, both in dry and aqueous settings.

Experiment	Number of fault(s)	Type of fault(s)	Fault sequence formation	1st fault formation location	MF distance (cm)	Shortening estimations (cm)	Sliding stopped
GD10	3	S-A-A	SEQ	SB1	25.1	3.7	Yes
GA10	2	S-A	SEQ	SB1	21.2	5	No
GD11	7	A-A-S-A-A-A-A	OOS	SB1	51.9	14.5	No
GA11	6	S-S-S-S-A-A	OOS	SB1	70.3	12.8	No
GD12	1	S	SEQ	SB1	18.8	2.2	Yes
GA12	3	S-S-S	OOS	SB2	35.6	4.8	No
GD07	4	S-A-A-A	OOS	SB2	39	6	Yes
GA07	5	S-S-S-S-A	SEQ	SB2	36.4	6.8	No
GD18	3	S-A-A	SEQ	SB1	27.6	4	No
GA18	3	S-A-A	SEQ	SB2	37.6	4.7	No
GD15	3	S-A-A	OOS	SB1	28.8	6.7	No
GA15	3	S-S-S	OOS	SB2	38.4	9	No
GD14	3	S-A-S	SEQ	SB1	31.3	3.8	No
GA14	4	S-A-A-A	SEQ	SB2	28.8	5.3	No

A: antithetic fault; S: synthetic fault; SEQ: sequence fault formation; OOS: out-of-sequence fault formation; SB: slope break; MF distance: morphological front.

zone with normal faults, (2) a translational zone with no fault, (3) a compressional zone corresponding to the morphological front with thrusts and (4) a damping zone with no fault but where tiny displacements of the superficial markers fade away, downslope (Fig. 3). Alternatively, but similarly, an additional translational-and-then-compressional zone may have formed downslope, usually upslope from the damping zone (*e.g.*, Figs. 3e–3h). Overall, most of the obtained slides propagated relatively rapidly from the very beginning of the experiments, with most of the displacements occurring during the first 12 h, and then progressively slowing down. Although they became particularly slow as time went on, it was rare for the sliding systems to completely stop over the course of the entire experiment (84 h). Nevertheless, the local and temporary slowing down or stopping of the displacements of some surficial markers were observed during all the experiments. For the sake of convenience, the results of each experiment are given as series providing direct comparisons for the dry and aqueous conditions.

5.1 Experiments without additional sand input

5.1.1 One slope break (G10 & G11 series)

For the G10 and G11 series of experiments, two slopes were imposed from either side of the single slope breaks. The angles of the plates were the same but the total lengths of the plates, upslope, differed (Figs. 2b and 2b' and Tab. 2). During sliding, both series provided the typical successive zones that are distributed from upslope to downslope (Figs. 5a–5c) or which displayed two translational and compressional zones (Fig. 5d). The final lengths of both the extensional and compressional zones are up to five times larger for the G11 experiments than for the G10 models (Figs. 5a–5c and Tab. 3). Accordingly, the distance of the morphological fronts, surfaces and volumes of the G11 sliding deposits are significantly larger than the G10 ones (Tab. 3). The G11 experiments also exhibit at least two times as many, or even more, thrust faults than the G10 experiments (Fig. 5). Folds, faulted folds and ramps occurred within the compressional zones and were responsible for the thickening of the sliding layer up to 2.5-cm in the GA11 experiment (Fig. 5d and Tab. 3). Overall, the G11 experiments underwent significantly more deformation than the G10 ones. For both series, the thrusts first appeared close to the slope breaks and then they developed either out-of-sequence during the G11 experiments or in sequence for the G10 experiments ones. In the GA11 experiment, a thrust also formed close to the very end of the device downslope.

Typically, the displacement record for the surficial markers shows that the sliding slowed down as time proceeded, usually decelerating at a higher rate in the dry experiments than in the corresponding aqueous models (Fig. 6). Correlatively, the maximum velocities were slightly higher for the dry experiments than for the aqueous ones (Tab. 3). In detail, the displacements of the markers located upslope underwent acceleration and deceleration (Fig. 6) that were observed to correlate in the compressional zones with the formation of new faults and local arrests of deformation along ramps, respectively. In addition, the final numbers of thrusts and folds in dry conditions are larger than for aqueous models, despite total shortening values that were, about the same or smaller for the dry experiments (Tab. 3).

5.1.2 Two slope breaks (G12 & G7 series)

On either side of both slope breaks and in-between, the plates for the G7 and G12 series were of the same length but exhibited different slopes (steeper slopes for the G07 models; Tab. 2). Slides also occurred in both series resulting in the typical distribution of the deformation zones from upslope to downslope (Figs. 5e–5h). Overall, the lengths, surfaces and volumes of the compressional zone(s) were larger for the G07 models than for the G12 ones (Tab. 3). Correlatively, the number of faults and folds and the shortening values were also

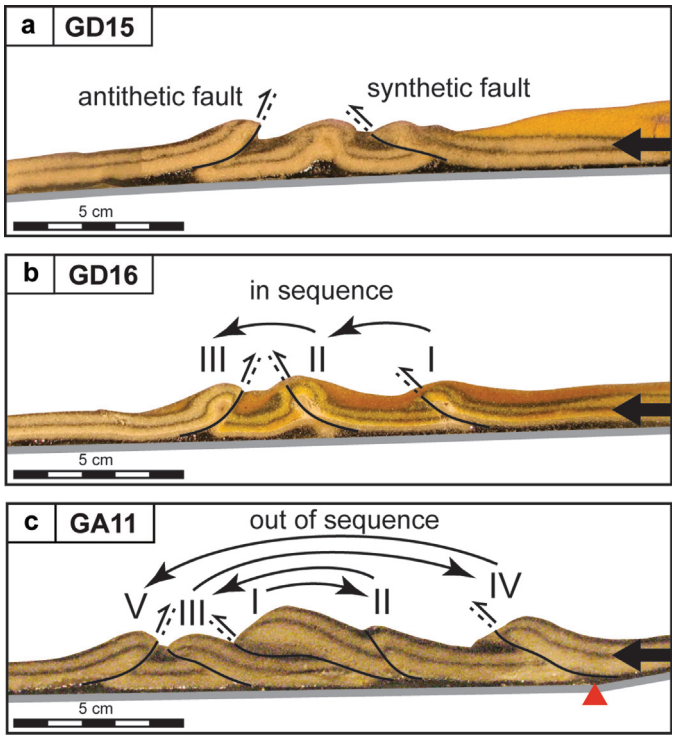

Fig. 4. Details of the final axial sections across the morphological fronts for the GD15, GA15 and GA11 experiments. The roman numerals indicate the order in which the faults appear. (a) Illustration of a synthetic *versus* an antithetic fault. (b) Illustration of faults formed in sequence. (c) Illustration of faults formed out of sequence. The black arrows on the right-hand side indicate the sliding direction. The roman numerals give the order of occurrence of the faults.

larger in the G07 compressional zones. In dry conditions, the distance of the morphological front is significantly larger for the GD07 experiment compared to the GD12 experiment, but the morphological front reached approximately the same locations in the GA07 and GA12 models under aqueous conditions (Tab. 3). For both series, the thrusts first appeared close to one of the slope breaks (more often SB2 than SB1) and then randomly developed either out-of-sequence or in sequence, independently of the controlled experimental conditions.

Under water, the final numbers of thrusts, the shortening values, and the distances of the fronts, surfaces, volumes and maximum thicknesses of the slides obtained are larger than – or, as large as – those obtained for the dry conditions (Fig. 5 and Tab. 3). The final distance of the morphological front for the GA12 experiment is roughly twice that than for the GD12 one, but it is only about the same as GD7 for GA7 (Fig. 5).

The analysis of the displacements of the superficial markers *versus* time (Fig. 6) reveals the same main results as for the G10-G11 series. Again, the highest velocities were reached within the first 12 h of the experiments, most often showing a velocity peak after 6 h (Fig. 6). The GD12 curve in Figure 6 illustrates that sliding was almost completely stopped starting from 36 h after the beginning of the experiment. Under water, the first faults were synthetic for both GA12 and GA07 and in dry conditions for GD12 (Tab. 3). For the GD07 experiment, the first fault was antithetic, indicating that these features hardly correlate with the controlled experimental conditions.

5.2 Experiments with additional sand input(s) (G18, G15 & G14 series)

The three series of experiments all involved two slope breaks in-between three plates of the same length and with the same slope values (Tab. 2). The G18 and G14 series underwent a single additional sand input of 150 g and 450 g, respectively, poured upslope (approximatively over plate P1) as soon as the experiments started. For the G15 series, a cumulative mass of 450 g of sand was also poured upslope; this was done as six successive inputs of 75 g of sand each periodically every 12 h.

Sliding was observed during all the experiments, again resulting in the typical distribution of the deformation zones from upslope to downslope (Fig. 7). Overall, the observed deformations have roughly the same intensities in the G14, G15 and G18 models (Fig. 7 and Tab. 3). The sizes, surfaces and volumes of the extensional and compressional zones, the morphological front distance and the number of structures in the compressional zone(s) are roughly the same for all of the experiments (Tab. 3). On main difference concerns the overall shortenings (displacements of the M1 marker, Tab. 3), which are larger in the G15 successive input models than the G18 and G14 single input experiments. Three to six reverse faults formed in sequence during the G14 and G18 experiments and out-of-sequence during the G15 ones. The first thrust was systematically synthetic and formed either in the vicinity of the SB1 slope break in dry conditions or in the vicinity of SB2 under water (Tab. 3).

In aqueous conditions, the GA14, GA15 and GA18 models also displayed larger lengths and surfaces for the compressional zones, larger volumes for the sliding deposits and, to a lesser extent, larger overall shortening values, compared to their dry counterparts (Fig. 7 and Tab. 3).

The G14 models exhibited the highest maximal displacement velocities for the superficial markers (Tab. 3 and Fig. 7). As for the experiments without additional sand input, the velocities for the G14 and G18 models progressively decreased with time after the maximum velocity was reached within the first six hours of the experiments. Conversely, the G15 models show much smaller velocity variations with almost linear displacement curves (Fig. 7). However, temporary decelerations and accelerations were recorded in all experiments of the three series. Some were observed to correlate with the stops of motions along the ramps and the creation of new faults, respectively, in the compressional zones. In addition, during the G15 models, some of the accelerations also correlate with some of the periodical sand inputs (Figs. 7b and 7d).

6 Interpretation and discussion

As sliding was observed in all the experiments, the results demonstrate that the gravitational driving forces systematically overcame the resisting forces (Locat and Lee, 2002), due to the presence of an underlying décollement layer along the slopes and a relatively thin initial sand layer. However, in the GD12

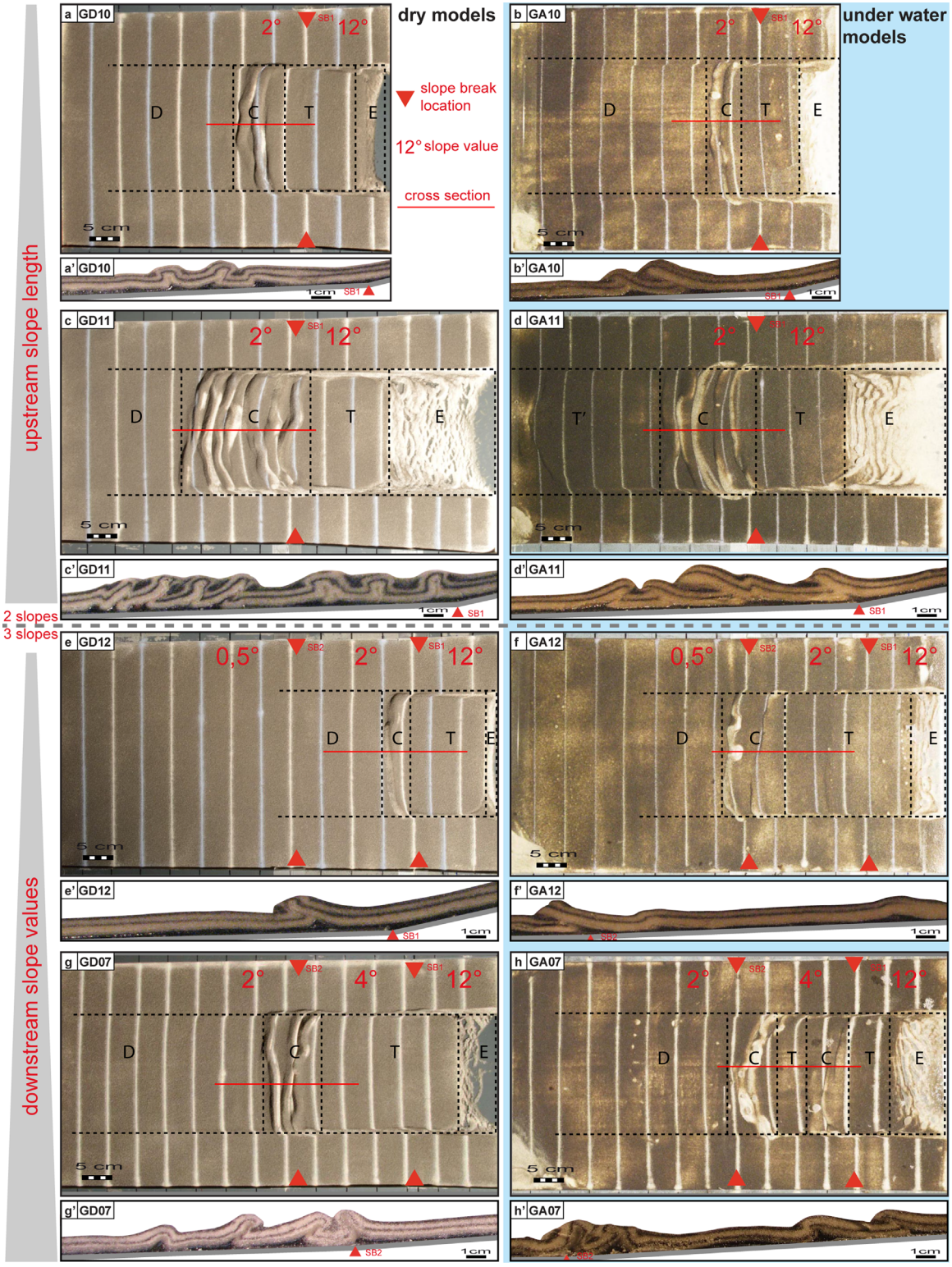

Fig. 5. Interpreted final surface views and corresponding axial cross-sections of the experiments without additional sand input. Same legend as Figure 3.

experiment, sliding stopped quite rapidly (36 h) showing that the strength of the thickened layer became dominant over the driving force during the course of the dry experiment. Together with the decelerations and then the accelerations of the sliding observed in all the experiments, this shows that the driving and resisting forces were about the same orders of magnitude. The starting experimental conditions mostly explored the influences of the various slope geometries (lengths and angle values), additional sand inputs and dry *versus* aqueous conditions on the dynamics of sliding.

6.1 Influence of slope geometry and slope breaks

Upslope, the slope lengths exert a significant influence on the slide dynamics. Longer upslope slopes result in larger displacements and, overall, more deformations in the systems than shorter upslope slopes (Figs. 5a–5d). An additional observation was that the first faults that formed often developed in the vicinity of a slope break. Given the experimental set-up, the distance separating the first fault from the upslope extremity of the device also places a limit on the upslope volume fraction of the slide, and therefore its mass fraction, which initially drove the sliding process. For instance, in the GD12 experiment where the first fault was roughly located above SB1, there was consistently less displacement and deformation in the end than for the GD07 model in which the first fault was near SB2, at a larger distance from the upslope box extremity (Figs. 5e and 5g). The G07 models also exhibited steeper slopes above plate P2 than the G12 models, which also result in larger final displacements and shortening values for the G7 experiments (Tab. 3 and Figs. 5e–5h). Indeed, steeper slopes favor sliding.

In addition, slope breaks localize the primary thrust system in most of the experiments. In models with two slope breaks, the first thrust faults essentially form at SB1 in the dry settings and at SB2 in the aqueous models. This localization of deformation at SB2 correlates with a further deformation propagation distance in aqueous conditions most of the time (Figs. 5 and 7). As a comparison, in the one-slope break models, the first thrust fault forms at the SB (*i.e.*, the G10 and G11 models) before propagating further. Therefore, a successive two-slope break system tends to localize compressional deformation zones at the furthest downslope slope break, and then it contributes to sliding over a longer runout distance. The geometry, and especially the number and distribution of the slope breaks, is a key parameter of propagation distance for sliding processes.

The G7 models are the only ones to show different results that might be due to two different causes. First, local variations in the sand layer thickness may induce a local strength variability into the system. A locally thinner layer is less resistant and favors rupture. Second, the distribution of the grains within a sand layer may also control the location of the emerging rupture zone. The development of thrusts either in sequence or out-of-sequence during sliding illustrates the effects of slope break location, sedimentary input and initial thickness variability. When the sand thickness is constant, the rupture zone only occurs where constraints are building up (in front of the sliding). However, when faults develop in an out-of-sequence way, this suggests that the thickness is not constant, and may favor the rupture and formation of faults behind the sliding, and not necessarily at the exact place where the constraints are accumulating.

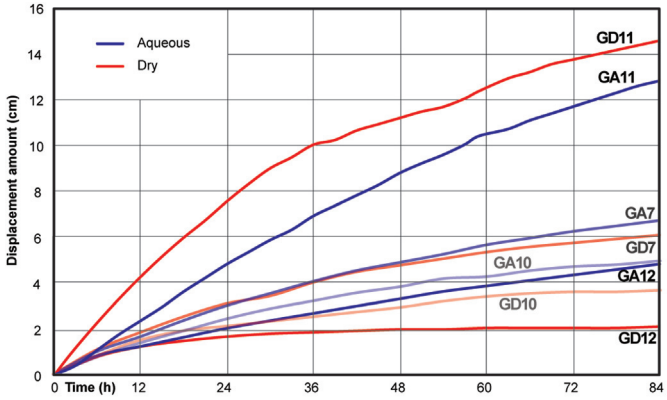

Fig. 6. Displacement of the surficial markers (M1, M2 and M3) with the time for the experiments without sand input.

Our observations with regards to the influence of the slope geometry on the sliding masses dynamics correlate with a previous study investigating the runout distances of debris avalanches offshore Martinique Island (Brunet *et al.*, 2017). Based on numerical simulations using two complementary depth-averaged thin-layer continuum models (Shaltop *versus* Hysea), our study shows that an accurate description of the complex topography is a crucial component in the dynamics and deposition of debris avalanches, perhaps even more so than its interaction with the water column.

6.2 Influence of hydrostatic pressure

It is challenging to run experiments on gravity-driven sliding processes under water. As far as we are aware, no such experiments have been performed before now (the present work), especially for the research topic of submerged slides. This is less due to the technical difficulties encountered when setting up an experimental device under water, and related more to quantifying and understanding the interactions between water and the other material used in the experiments.

At a given depth, the hydrostatic pressure corresponds to the water column between this depth and the surface. It is 0.4 times the lithostatic pressure and leads to rock densities up to 2500 kg/m^3. Interstitial pressures higher than the hydrostatic pressure may be related to various mechanisms such as rapid sediment compaction, deformation or dehydration because of the pressure and temperature variations. In order to take interstitial pressure into account in the strength calculation, it is necessary to modify the Mohr–Coulomb criteria (1) as follows (von Terzaghi, 1923):

$$\tau = c + (\sigma - p)\tan\delta, \quad (1)$$

where τ is the shear stress, c is the cohesion, σ is the normal stress, p is the interstitial pressure and $\sigma - p$ is defined as the effective normal stress σ' and δ is the friction angle. In addition, the main effective stresses are $\sigma 1' = \sigma 1 - p$ and

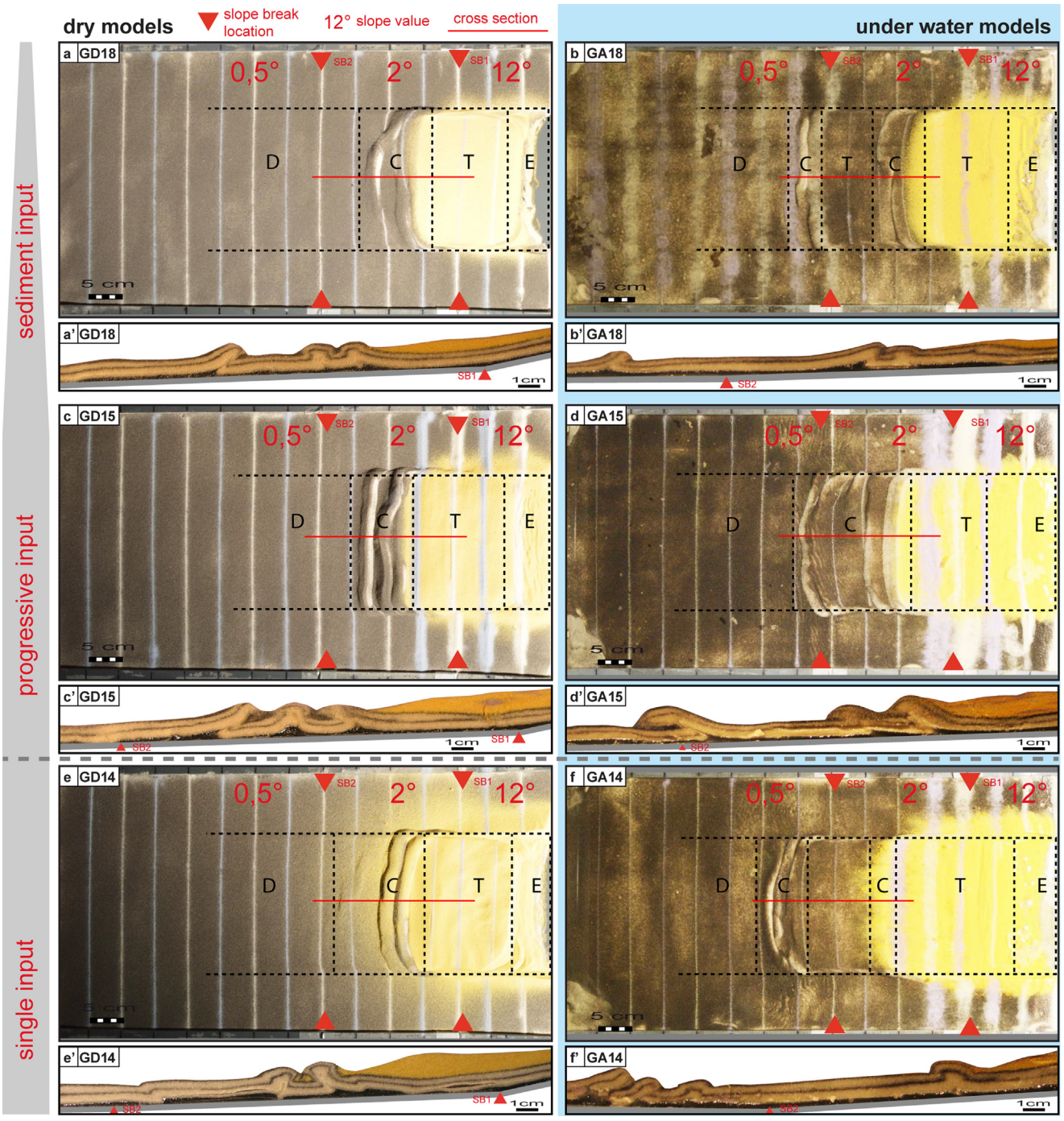

Fig. 7. Interpreted final surface views and corresponding axial cross-sections of the experiments with additional sand input. Same legend as Figure 3.

$\sigma 3' = \sigma 3 - p$. Thus, with fluid pressure, the effective strength $\sigma 1 - \sigma 3$ decreases to give $\sigma 1' - \sigma 3'$, which facilitates the deformation and sliding (Fig. 8).

Our experiments have demonstrated significant differences between the aqueous and dry models (Figs. 5 and 6). Most of our results clearly show that deformation propagates further in aqueous models compared to the dry counterparts (Tab. 3 and Figs. 6 and 9), which is consistent with the principle stated above. Therefore, we assume that the sand cohesion in our models is very low and the hydrostatic pressure induced by the water column above the sand level is both a facilitator mechanism and a catalyst for deformation propagation.

Lastly, contrary to sediment inputs that increase locally as well as temporary gravity constraints on sliding – and thus driving forces –, the hydrostatic pressure permanently induces a decrease in the effective strength $\sigma 1' - \sigma 3'$ thereby facilitating the movement on faults that favors sliding and deformation. This is correlated with the continuously progressing sliding in

aqueous models compared to dry ones. Only the G11 models show an opposite trend, but they were characterized by higher gravity forces (longer and steeper slopes) (Figs. 6 and 9).

The increase of deformation facilitated by fluid overpressure in sliding processes has been extensively studied and demonstrated, through either field observations or experimental modeling with compressed air as a pore fluid in sandbox models (Cobbold and Castro, 1999; 2001, 2009; Mourgues and Cobbold, 2003; Mourgues *et al.*, 2009). Among the mechanisms producing an increase in fluid volume are thermal dilation, mineralogical transformation and hydrocarbon generation (Osborne and Swarbrick, 1997).

In the previous paragraph, we notice that for steeper and longer slopes upslope (*i.e.*, the G12, G10, G7 and G11 models, respectively), the propagation distance increases correlatively to the cumulated amount of shortening (Tab. 3 and Fig. 5), illustrating a growing gravity power in these models. Similarly, it appears that a steeper slope over a long distance (*i.e.*, G11 models) has more impact in terms of shortening and propagation distance rather than the decrease in the effective strength $\sigma 1'$–$\sigma 3'$ (Tab. 3 and Fig. 5). This demonstrates that increasing slope angles favorably affect the sliding propagation distance, however, it also shows that the length of the slopes may modify the slide features so that when the slopes are longer, the driving gravity power for sliding becomes greater. The hydrostatic pressure and the induced decrease in the effective strength in the sand layer facilitate the movement on faults; this was observed experiment GA11 where there are fewer reverse faults in the compressional zone than in GD11, but the fault throw is larger.

Our experiments demonstrate the large control exerted by the system's geometry over the sliding dynamics and the hydrostatic pressure with respect to the organization of the faults.

6.3 Influence of sediment inputs

Regardless of the type of sedimentary input, our experiments have demonstrated that this input represents a driving mechanism rather than a triggering mechanism as per the sliding dynamics. With or without inputs, sliding initiates at the very beginning of the experiments. However, sedimentary inputs allow deformations to propagate over a longer distance. During the 12 h separating each input, the displacements may significantly slow down to the point where it appears that the sliding is about to stop.

The shortening/displacement rate – and therefore the induced deformation – increases in the following order: the G18, G14 and G15 models. This observation suggests that regular sediment inputs deposited upslope have more impact in terms of deformation of the upper slope (*i.e.*, displacement rate) than those deposited all at once (Tab. 3 and Figs. 7 and 9). In addition, shortening is most often higher in aqueous models (Tab. 3 and Figs. 7 and 9), and is related to hydrostatic pressure which permanently causes a decrease in the effective strength $\sigma 1'$–$\sigma 3'$ and favors sliding and deformation.

With regards to the propagation distance, it is important to take the formation of locking fronts during sliding into account, as they tend to decrease the runout distances. These fronts appear during most of the experiments and decrease the propagation of the faults both locally and temporarily, whereas the upslope translation is still progressing. Therefore, the stresses accumulate at the fronts and once they exceed the resistivity stresses, the locking front gives way under stress and the sliding propagates again. This "unlocking" process leads to a slight increase in velocity.

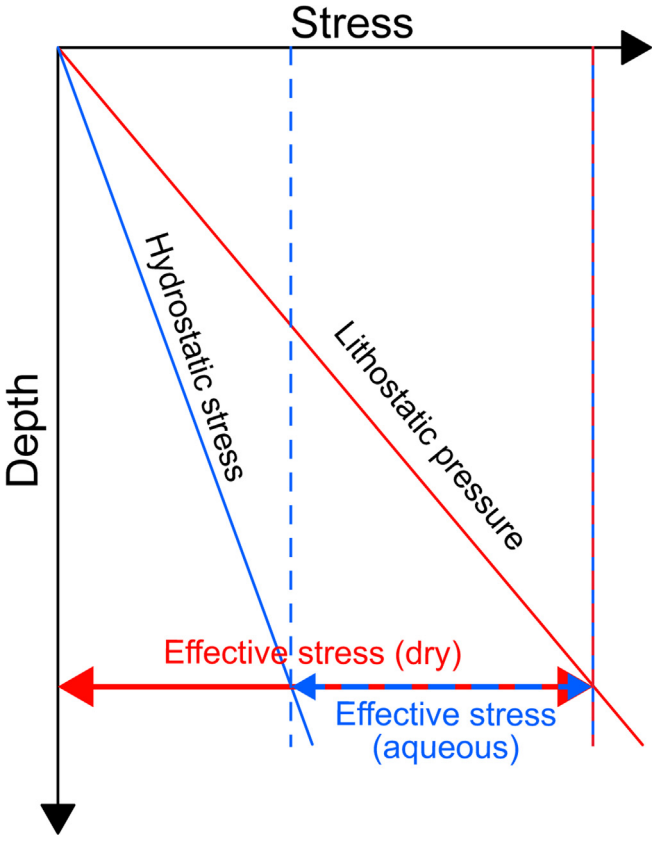

Fig. 8. Illustration of the effect of pore-fluid pressure.

In addition, the initial upslope sediment inputs in the G18 and G14 models (three times larger in G18 than in G14), result in more shortening in the G14 model than in the G18 model (approximately 15% higher, in both the dry and aqueous models). Similarly, the propagation distance is longer in both aqueous models compared to the dry ones (almost doubled between GA14 and GS14) (Tab. 3 and Figs. 7 and 9).

As previously mentioned, either with or without sediment inputs, it is common for sliding to not stop in aqueous conditions. However, in dry models, only some of the models without sediment inputs stop sliding (*i.e.*, GG10 and G12 models). Periodic inputs make it possible to maintain sliding over time (Fig. 10). As expected, this shows that a regular input of sediments in the sliding process is a driving mechanism, but it is even more significant when its effects are combined with those of hydrostatic pressure (Fig. 10). In addition, the sliding process stops in the following order: GS12, GS10, GS18 and GS14. These examples clearly illustrate that the initial sediment inputs result in additional driving stresses compared to models without sediment inputs, but they do not prolong sliding for as long as the regular inputs do. Indeed, during sliding, two processes occur: (1) the downslope series become thicker because of shortening, hence they become stronger;

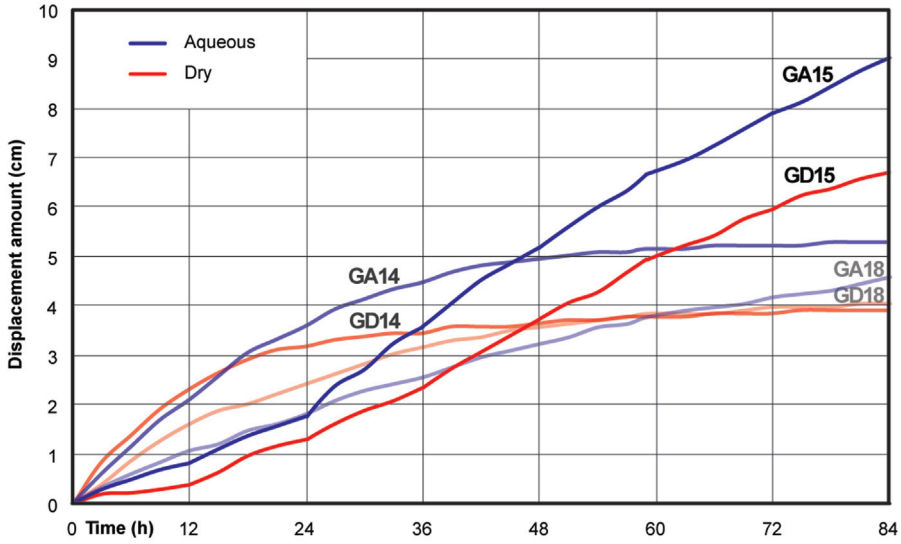

Fig. 9. Displacement of the surficial markers (M1, M2 and M3) with the time for the experiments with sand input.

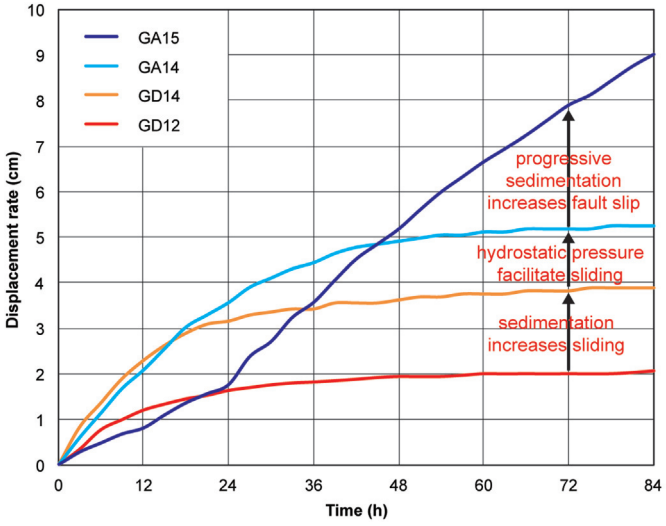

Fig. 10. Comparison of the displacements of the first marker (M1) for the GD12, GD14, GA14 and GA15 models.

(2) the length of the mid-slope sliding block becomes shorter. Therefore, the driving force decreases while the resisting force increases, leading to slow down or even a stop in deformation. By adding new sediments in the upslope area, the sliding block retrieves its original length, "restarting" the driving force (see Fig. 11).

This positive correlation between sedimentary supply and deformation intensity is also observed at different scales and settings. For instance, the gravity-driven deformation observed at the Niger Delta has been widely investigated and related to overpressured shales (*e.g.*, Damuth, 1994; Wu *et al.*, 2000; Bilotti and Shaw, 2005; Corredor *et al.*, 2005; Briggs *et al.*, 2006; Cobbold *et al.*, 2009; Mourgues *et al.*, 2009; Maloney *et al.*, 2010), and has also been associated with the spatial variations in the sedimentary supply that cause spatial variations in the deformation intensity and rate: when the progradation length is longer, the intensity of the gravity-driven deformation is higher (Rouby *et al.*, 2011).

6.4 Deformation quantification

Based on previous observations and interpretations, our experiments have highlighted three main factors contributing to the sliding deformation: slope geometry, hydrostatic pressure and sediment supply. A large number of studies have investigated the influence of the slope geometry on the sliding propagation, *i.e.*, focusing on physical parameters such as the slope steepness and the type of décollement layers (Cobbold and Castro, 1999; Cobbold *et al.*, 2009; Mourgues and Cobbold, 2003; Mourgues *et al.*, 2009), showing the sliding potential of slopes (inclined only a few degrees) when associated with a specific décollement layer (*i.e.*, salt tectonics, Fort *et al.*, 2004; Brun and Fort, 2011). In the present study, we go further by demonstrating how slope breaks between the slope portions can localize the formation of the first thrusts and their propagation depending on the driving forces at play. Our experimental observations fully support another study demonstrating how submarine slope breaks constrain the runout of the debris avalanches offshore Martinique Island using a numerical simulation (Brunet *et al.*, 2017). Therefore, the slope geometry could be considered as a preconditional and triggering factor for sliding when combined with other factors such as sediment loading, seismicity or specific décollement layers. With regards to the hydrostatic pressure, our models have clearly demonstrated its catalyst effect on sliding mobility over time, followed by the capacity to increase the sliding and deformation runout distance (Figs. 6 and 9). Numerical simulations on debris avalanches when they entered sea were also used to test the involvement of hydrostatic pressure on sliding dynamics, but the results showed that it is complex topographies rather than hydrostatic pressure that seem to have an impact on gravity-sliding processes (Brunet *et al.*, 2017). Lastly, the experiments with sediment inputs demonstrated that irrespective of the type of sedimentary input and the experimental conditions (dry or aqueous),

the inputs represent a driving mechanism and not a triggering mechanism with regards to the sliding dynamics. With or without inputs, sliding is initiated from the very beginning of the experiments (Figs. 6 and 9). However, inputs allow deformations to propagate over longer distances (Figs. 9 and 10). Sediment inputs may also trigger temporary sliding accelerations just after deposition resulting in increased deformation within the sliding mass. This positive correlation between high sediment input and gravity-driven deformation has been widely recognized at different geological scales and settings, *i.e.*, deltaic fronts or glacial continental margins (Adams and Roberts, 1993; Imbo *et al.*, 2003; Bryn *et al.*, 2005; Leynaud *et al.*, 2007; Rouby *et al.*, 2011), and involves the generation of excess pore pressure. In the present study, the experiments have also shown that a regular supply of sediment in the sliding process is the major driving mechanism, but it is even more significant when combined with another catalytic/driving mechanism such as hydrostatic pressure (Fig. 10).

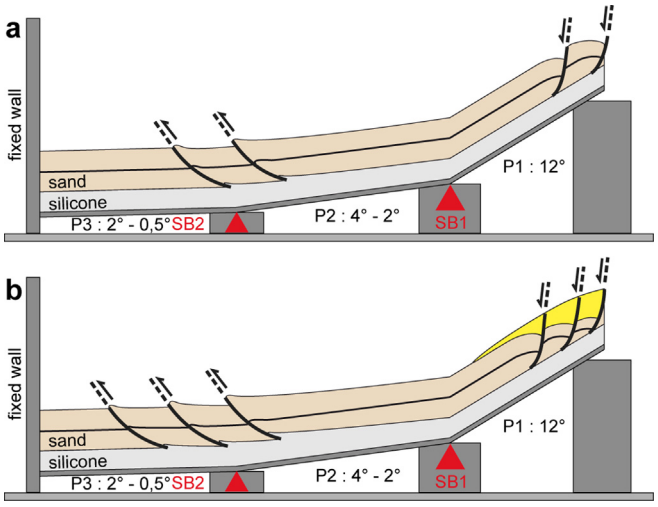

Fig. 11. Schematic cross-section showing the effect of sedimentation in the amount of the deformation in experiments (a) without sedimentation during deformation and (b) with sedimentation during deformation.

6.5 Comparison with the natural setting: offshore Martinique Island

6.5.1 Geometry and structures

The geometric characteristics (thickness and length of the deposit, slope, sediment inputs, etc.) of the experimental device have been set up based on the interpreted marine geophysical data (Brunet *et al.*, 2016) acquired offshore Martinique (Deplus *et al.*, 2001, 2002; Le Friant *et al.*, 2003a; Fig. 1).

With regards to the structures, the morphological front identified using bathymetric and seismic reflection data (Fig. 1) may be correlated to the formation of multiple thrusts as observed in our experimental models (Fig. 12). This surficial structure is related to the deep frontal ramp highlighted in Brunet *et al.* (2016), and as is typical of frontally emergent slides (Frey-Martínez *et al.*, 2006), it is similar to the frontal ramp observed in some of our models (Fig. 4c). In addition, the thrusts and folds system described in the distal part of the slide are also systematically observed in our models and can be compared to those observed on seismic profiles (Fig. 1). The resolution of the seismic data is limited compared to the experimental cross-sections, and therefore caution should be taken when comparing the structures, *e.g.*, fold structures may be confused with diffraction hyperbola for instance. Thus, analogue modelling can also potentially provide structural information when the current available data cannot. Lastly, microstructures identified on the drilled cores, such as micro-faults, inclined bedding or reverse grading (Brunet *et al.*, 2016), indicate major compressional movements that may be associated with either large-scale folds (straight, overturned or bedded), or thrusts with variable strikes and dips (Fig. 12).

As previously mentioned, the second slope break locates the thrust formation (especially in aqueous conditions) and the subsequent propagation of the deformation downslope. This is also observed in the real context, with the main front located approximately 25 km downslope from the second slope break. In addition, the maximum thickness may reach 500 m, which lies perfectly within the measurement range for the modeled slides. Frontally emergent slides are also characterized by a surficial morphological front, a deep frontal ramp and a distal translational sliding mass (Frey-Martínez *et al.*, 2006). These additional features were not reproduced in the laboratory, only a few frontal ramps appear in the GA11 and GA15 models. In nature, these ramps do not exceed a height of 150 m, whereas they can reach 0.5 to 1 cm in the models (equivalent to 500–1000 m high). It is significant that a difference of one order of magnitude is observed; this shows that the models do not exactly reproduce what is observed in nature, although it is similar in other respects (Fig. 12). Nevertheless, this difference can be explained by the unique oversized décollement layer in the models compared to the multiple ones that probably occur in nature (Lafuerza *et al.*, 2014; Hornbach *et al.*, 2015; Mencaroni *et al.*, 2020; Knappe *et al.*, 2020; Llopart *et al.*, 2021). Therefore, in the laboratory, the formation of frontal ramps will involve the whole overlying sand stratigraphic interval (1 cm-thick) whereas in nature, the layout of the potential multi-décollement layers will involve the displacement of thinner stratigraphic intervals, resulting in smaller frontal ramps. Although observed in the seismic data (Fig. 1c), a distal deformed unit beyond the frontal ramp is missing in our models; this may be due to a lack of sufficient inertial energy allowing the slide mass to emerge beyond a stratigraphic level and to be translated over a long distance (Frey-Martínez *et al.*, 2006).

6.5.2 Kinematics

The submarine landslide occurring in Martinique is not constrained yet in terms of timing. It might have been emplaced in few hours or in few days, or could even be still active today, either continuously or intermittently. The scenario proposed by Brunet *et al.* (2016) suggests a submarine landslide triggered by the emplacement of debris avalanches next to a major volcano flank-collapse event dated at 127 ka and reactivated at least once at 36 ka (Solaro *et al.*, 2020; Boudon and Balcone-Boissard, 2021) by successive debris avalanche deposits loading the submarine volcano slope. As demonstrated by some experiments, a sudden sediment input

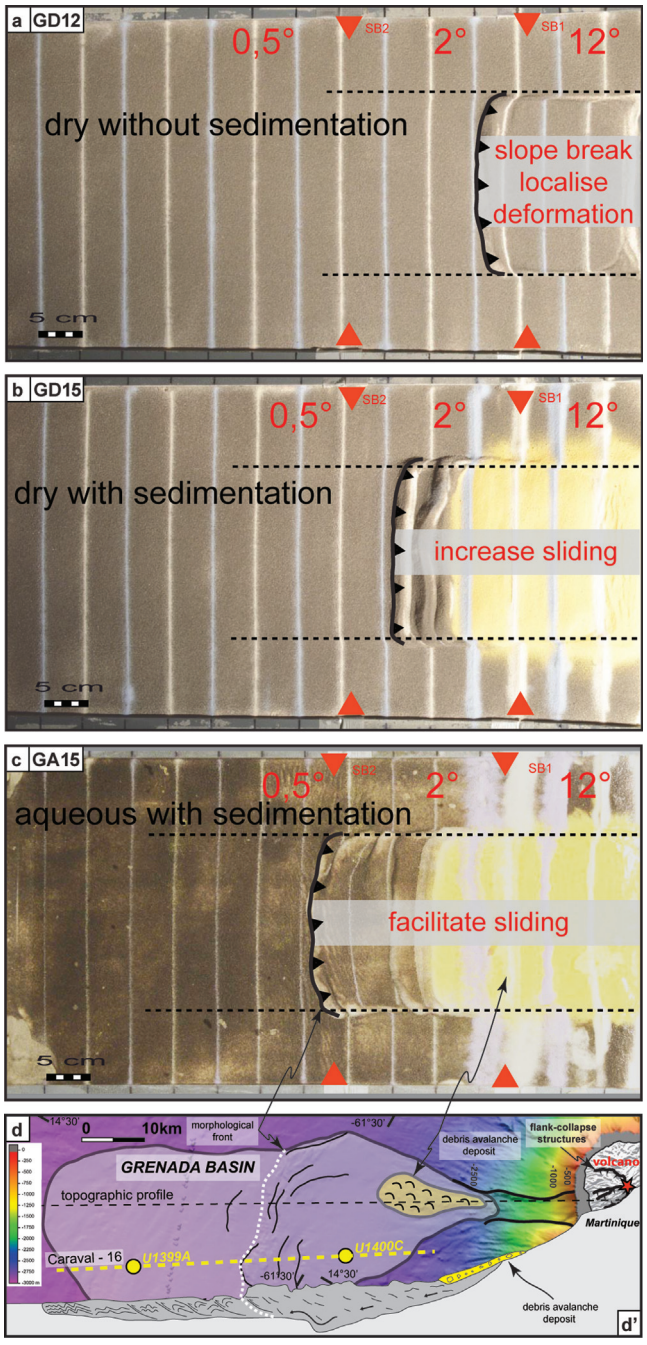

Fig. 12. Summary illustration comparing the models with two slope breaks and the related observations, in (a) dry conditions without sedimentation (GD12), (b) dry conditions with periodical sedimentation (GD15) and (c) aqueous conditions with periodical sedimentation (GA15). These experimental observations are compared in (d) with the natural setting observations (to the west, offshore Martinique Island). (dd') A schematic cross-section of the submarine landslide deposit (light gray deposit) and the overlying debris avalanche deposit (dark gray) (modified from Brunet *et al.*, 2016).

can temporarily accelerate or reactivate a slide, which is compatible with the proposed scenario. Moreover, the experiments showed that all types of sediment inputs contribute to sliding process in one way or another. Applied to natural conditions, these inputs may not only correspond to debris avalanches but also to turbidity currents, debris flows or regular large-scale Grenada basin sedimentation.

So far, there are no temporal constraints with regards to the dynamics of the submarine landslide from Martinique Island, but the experiments do provide some kinematic proxies. Slides are still slightly progressing in most parts of the models after 84 h (*i.e.*, the end of the experiment), but we can infer that the speed of these displacements is close to zero. Applied to natural conditions, our experiments suggest that the last and smaller volcano flank-collapse event, recently dated at 36 ka (Solaro *et al.*, 2020) and the related debris avalanche volume estimated at 2 km^3 (Le Friant *et al.*, 2003a), would not have allowed the slide to propagate up to the point where it is observed today. We show that the first inputs, *i.e.*, debris avalanches from the first flank-collapse event, dated at 127 ka (Germa *et al.*, 2011) and with an estimated volume between 14.7 km^3 and 25 km^3 (Le Friant *et al.*, 2003a; Germa *et al.*, 2015), tend to have higher impacts on the sliding propagation, especially when they involve large volumes (G14 model *vs.* G18 model). When applied to the natural system, these results suggest that the last and smaller flank-collapse event might have had a smaller impact, if any, on the submarine landslide deposit. This observation supports studies that consider the first volcano flank-collapse event and the related debris avalanche as not only the largest in Montagne Pelée's geological history (Le Friant *et al.*, 2003a, b; Boudon *et al.*, 2007; Boudon and Balcone-Boissard, 2021; Solaro *et al.*, 2020) but also the one responsible for the large-scale submarine landslide identified offshore Martinique Island (Brunet *et al.*, 2016).

7 Conclusions

The complex submarine slope to the west of Martinique Island, in the Lesser Antilles arc, exhibits various types of gravity-driven submarine landslides and debris avalanches. Laboratory modelling experiments designed to test the emplacement dynamics in either dry or aqueous conditions, as well as to assess the respective contributions of slope geometry, hydrostatic pressure and sediment input indicate that:

- the slope geometry controls the distribution and propagation of the deformation patterns. In particular, the slope breaks control the location of the first thrusts. Further propagation is observed in the case of multiple slope breaks;
- with increasing slope steepness and length, the influence of gravity is higher and the sliding goes further;
- hydrostatic pressure decreases the effective strength, thereby facilitating the movement on faults and favoring sliding and deformation in dry conditions;
- based on the sliding dynamics, it is more likely that sediment inputs are a driving mechanism and not a triggering mechanism. Sediment inputs increase the gravity forces and sliding deformation. However, they allow deformations to propagate for longer distances;
- when occurring only periodically, sediment inputs can temporally and locally accelerate sliding.

Funding

Funding for this research was provided by the INSU, ANR CARIB and the Bureau IODP-France.

Acknowledgments. The authors wish to thank S. Mullin for proofreading the English content. They are also grateful to Bruno Vendeville for his valuable comments allowing to significantly improve the manuscript, being one of his last contributions for our community.

References

Adams CE, Roberts HH. 1993. A model of the effects of sedimentation rate on the stability of Mississippi Delta sediments. *Geo-Marine Letters* 13(1): 17–23.

Albertz M, Beaumont C, Shimeld JW, Ings SJ, Gradmann S. 2010. An investigation of salt tectonic structural styles in the Scotian Basin, offshore Atlantic Canada: 1. Comparison of observations with geometrically simple numerical models. *Tectonics* 29(4). https://doi.org/10.1029/2009TC002539.

Barrier L, Nalpas T, Gapais D, Proust J-N. 2013. Impact of synkinematic sedimentation on the geometry and dynamics of compressive growth structures: Insights from analogue modelling. *Tectonophysics* 608: 737–752.

Bilotti F, Shaw JH. 2005. Deep-water Niger Delta fold and thrust belt modeled as a critical-taper wedge: The influence of elevated basal fluid pressure on structural styles. *AAPG Bulletin* 89(11): 1475–1491.

Borgia A. 1994. Dynamic basis of volcanic spreading. *Journal of Geophysical Research* 99(B9): 17791–17804.

Borgia A, Treves B. 1992. Volcanic plates overriding the ocean crust: Structure and dynamics of Hawaiian volcanoes. *Geological Society, London, Special Publications* 60(1): 277–299.

Borgia A, Ferrari L, Pasquarè G. 1992. Importance of gravitational spreading in the tectonic and volcanic evolution of Mount Etna. *Nature* 357(6375): 231–235.

Boudon G, Balcone-Boissard H. 2021. Volcanological evolution of Montagne Pelée (Martinique): A textbook case of alternating Plinian and dome-forming eruptions. *Earth-Science Reviews* 221: 103754.

Boudon GA, Le Friant B, Villemant B, Viode J-P. 2005. Martinique. In: Lindsay JM *et al.*, eds. *Volcanic Atlas of the Lesser Antilles*. Trinidad and Tobago: University of the West Indies, Seismic Research Unit, pp. 65–102.

Boudon G, Le Friant A, Komorowski J-C, Deplus C, Semet MP. 2007. Volcano flank instability in the Lesser Antilles Arc: Diversity of scale, processes, and temporal recurrence. *Journal of Geophysical Research* 112(B8): B08205. https://doi.org/10.1029/2006JB004674.

Bouysse P, Westercamp D, Andreieff P. 1990. The Lesser Antilles arc. In: Moore JC, Mascle A, *et al.*, eds. *Proceedings of the Ocean Drilling Program. Scientific Results 110*, pp. 29–44.

Briggs SE, Davies RJ, Cartwright JA, Morgan R. 2006. Multiple detachment levels and their control on fold styles in the compressional domain of the deepwater West Niger Delta. *Basin Research* 18(4): 435–450.

Brun JP, Choukroune P. 1983. Normal faulting, block tilting, and décollement in a stretched crust. *Tectonics* 2(4): 345–356.

Brun JP, Fort X. 2011. Salt tectonics at passive margins: Geology *versus* models. *Marine and Petroleum Geology* 28(6): 1123–1145.

Brunet M. 2015. Caractérisation des processus d'instabilité affectant les îles volcaniques : application au volcan de la Montagne Pelée en Martinique à partir de l'exploitation des forages de l'Expédition IODP 340. Thèse de doctorat, Institut de Physique du Globe de Paris.

Brunet M, Le Friant A, Boudon G, Lafuerza S, Talling P, Hornbach M, *et al.* 2016. Composition, geometry, and emplacement dynamics of a large volcanic island landslide offshore Martinique: From volcano flank-collapse to seafloor sediment failure? *Geochemistry, Geophysics, Geosystems* 17(3): 699–724.

Brunet M, Moretti L, Le Friant A, Mangeney A, Nieto EDF, Bouchut F. 2017. Numerical simulation of the 30–45 ka debris avalanche flow of Montagne Pelée volcano, Martinique: From volcano flank collapse to submarine emplacement. *Natural Hazards* 87(2): 1189–1222.

Bryn P, Berg K, Forsberg CF, Solheim A, Kvalstad TJ. 2005. Explaining the Storegga slide. *Marine and Petroleum Geology* 22 (1-2): 11–19.

Burollet PF. 1975. Tectonique en radeaux en Angola. *Bulletin de la Société Géologique de France* 7(4): 503–504.

Byrne PK, Holohan EP, Kervyn M, van Wyk de Vries BVW, Troll VR, Murray JB. 2013. A sagging-spreading continuum of large volcano structure. *Geology* 41(3): 339–342.

Cassidy M, Trofimovs J, Watt SFL, Palmer MR, Taylor RN, Gernon TM, *et al.* 2014. Multi-stage collapse events in the South Soufrière Hills, Montserrat as recorded in marine sediment cores. *Geol. Soc. London* 39: 383–397.

Cloos E. 1968. Experimental analysis of Gulf Coast fracture patterns. *AAPG Bulletin* 52(3): 420–444.

Cobbold PR, Szatmari P. 1991. Radial gravitational gliding on passive margins. *Tectonophysics* 188: 249–289.

Cobbold PR, Castro L. 1999. Fluid pressure and effective stress in sandbox models. *Tectonophysics* 301(1-2): 1–19.

Cobbold P, Rossello E, Vendeville B. 1989. Some experiments on interacting sedimentation and deformation above salt horizons. *Bulletin de la Société Géologique de France* (3): 453–460.

Cobbold PR, Meisling KE, Mount VS. 2001. Reactivation of an obliquely rifted margin, Campos and Santos basins, southeastern Brazil. *AAPG Bulletin* 85(11): 1925–1944.

Cobbold PR, Clarke BJ, Løseth H. 2009. Structural consequences of fluid overpressure and seepage forces in the outer thrust belt of the Niger Delta. *Petroleum Geoscience* 15(1): 3–15.

Cohen HA, Hardy S. 1996. Numerical modelling of stratal architectures resulting from differential loading of a mobile substrate. *Geological Society, London, Special Publications* 100 (1): 265–273.

Cohen HA, McClay K. 1996. Sedimentation and shale tectonics of the northwestern Niger Delta front. *Marine and Petroleum Geology* 13 (3): 313–328.

Corredor F, Shaw JH, Bilotti F. 2005. Structural styles in the deep-water fold and thrust belts of the Niger Delta. *AAPG Bulletin* 89(6): 753–780.

Crans W, Mandl G, Haremboure J. 1980. On the theory of growth faulting: A geomechanical delta model based on gravity sliding. *Journal of Petroleum Geology* 2(3): 265–307.

Crutchley GJ, Karstens J, Berndt C, Talling PJ, Watt SFL, Vardy ME, *et al.* 2013. Insights into the emplacement dynamics of volcanic landslides from high resolution 3D seismic data acquired offshore Montserrat, Lesser Antilles. *Mar. Geol.* 335: 1–15. https://doi.org/10.1016/j.margeo.2012.10.004.

Damuth JE. 1994. Neogene gravity tectonics and depositional processes on the deep Niger Delta continental margin. *Marine and Petroleum Geology* 11(3): 320–346.

Davy P, Cobbold PR. 1991. Experiments on shortening of a 4-layer model of continental lithosphere. *Tectonophysics* 188: 1–25.

Delcamp A, van Wyk de Vries B, James MR. 2008. The influence of edifice slope and substrata on volcano spreading. *Journal of Volcanology and Geothermal Research* 177(4): 925–943.

Delcamp A, van Wyk de Vries BVW, James MR, Gailler LS, Lebas E. 2012. Relationships between volcano gravitational spreading and magma intrusion. *Bulletin of Volcanology* 74(3): 743–765.

DeMets C, Jansma PE, Mattioli GS, Dixon TH, Farina F, Bilham R, *et al.* 2000. GPS geodetic constraints on Caribbean-North America plate motion. *Geophysical Research Letters* 27: 437–440.

Deplus C, Le Friant A, Boudon G, Komorowski J-C, Villemant B, Harford C, *et al.* 2001. Submarine evidence for large-scale debris avalanches in the Lesser Antilles arc. *Earth and Planetary Science Letters* 192(2): 145–157.

Deplus C, Le Friant A, Boudon G, Komorowski J-C, Sparks S, Harford C. 2002. Numerous DADs off the southern part of Monserrat revealed by recent oceanographic cruises. In: Paper presented at *International Congress on Montagne Pelée 1902–2002, IPGP-INSU-IAVCEI, Martinique Island, 12–16 May.*

Déramond J. 1979. Déformation et déplacement des nappes : exemple de la nappe de Gavarnie (Pyrénées centrales). Thèse, Faculté de Science, Toulouse, 409 p.

Doust H, Omatsola E. 1990. *AAPG Memoir* 48: 201–238.

Faugère E, Brun JP. 1984. Modélisation expérimentale de la distension continentale. *Comptes Rendus de l'Académie des Sciences, Série II* 299: 365–370.

Feuillet N, Leclerc F, Tapponnier P, Beauducel F, Boudon G, Le Friant A, *et al.* 2010. Active faulting induced by slip partitioning in Montserrat and link with volcanic activity: New insights from the 2009 GWADASEIS marine cruise data. *Geophys. Res. Lett.* 37: L00E15. https://doi.org/10.1029/2010GL042556.

Fletcher P, Gay NC. 1971. Analysis of gravity sliding and orogenic translation: Discussion. *Geological Society of America Bulletin* 82 (9): 2677–2682.

Fort X, Brun JP, Chauvel F. 2004. Salt tectonics on the Angolan margin, synsedimentary deformation processes. *AAPG Bulletin* 88 (11): 1523–1544.

Frey-Martínez J, Cartwright J, James D. 2006. Frontally confined *versus* frontally emergent submarine landslides: A 3D seismic characterisation. *Marine and Petroleum Geology* 23: 585–604.

Gaullier V, Vendeville BC. 2005. Salt tectonics driven by sediment progradation: Part II – Radial spreading of sedimentary lobes prograding above salt. *AAPG Bulletin* 89(8): 1081–1089.

Ge H, Jackson MPA, Vendeville BC. 1997. Kinematics and dynamics of salt tectonics driven by progradation. *American Association of Petroleum Geologists Bulletin* 81: 398–423.

Gemmer L, Ings SJ, Medvedev S, Beaumont C. 2004. Salt tectonics driven by differential sediment loading: Stability analysis and finite- element experiments. *Basin Research* 16(2): 199–218.

Gemmer L, Beaumont C, Ings SJ. 2005. Dynamic modelling of passive margin salt tectonics: Effects of water loading, sediment properties and sedimentation patterns. *Basin Research* 17(3): 383–402.

Germa A, Quidelleur X, Lahitte P, Labanieh S, Chauvel C. 2011. The K-Ar Cassignol–Gillot technique applied to western Martinique lavas: A record of Lesser Antilles arc activity from 2 Ma to Mount Pelée volcanism. *Quaternary Geochronology* 6(3): 341–355.

Germa A, Lahitte P, Quidelleur X. 2015. Construction and destruction of Mount Pelée volcano: Volumes and rates constrained from a geomorphological model of evolution. *J. Geophys. Res. Earth Surf.* 120: 1206–1226. https://doi.org/10.1002/2014JF003355.

Graham RH. 1981. Gravity sliding in the Maritime Alps. In: McClay KR, Price NJ, eds. *Thrust and Nappe Tectonics*. Geol. Soc. London Spec. Publ. 9, pp. 335–352.

Haack RC, Sundararaman P, Diedjomahor JO, Xiao H, Gant NJ, May ED, *et al.* 2000. Chapter 16: Niger Delta Petroleum Systems, Nigeria. *AAPG Memoir* 73: 213–231.

Hornbach MJ, Manga M, Genecov M, Valdez R, Miller P, Saffer D, *et al.* 2015. Permeability and pressure measurements in Lesser Antilles submarine slides: Evidence for pressure-driven slow-slip failure. *Journal of Geophysical Research: Solid Earth* 120(12): 7986–8011.

Hsü KJ, Siegenthaler C. 1969. Preliminary experiments on hydrodynamic movement induced by evaporation and their bearing on the dolomite problem. *Sedimentology* 12(1-2): 11–25.

Hubbert MK. 1937. Theorie of scale models as applied to the study of geologic structures. *Bull. Geol. Soc. Am.* 48: 1459–1520.

Hubbert MK, Rubey WW. 1959. Role of fluid pressure in mechanics of overthrust faulting. I. Mechanics of fluid-filled porous solids and its application to overthrust faulting. *Geol. Soc. Am. Bull.* 70: 115–166.

Hudlestone PJ. 1976. Recumbent folding in the base of the Barnes ice cap, Baffin Island, Norwest Territories, Canada. *Geol. Soc. Amer. Bull.* 70: 115–116.

Hudlestone PJ. 1977. Similar folds, recumbent folds and gravity Tectonics in ice and rocks. *J. Geol.* 85: 113–122.

Hudlestone PJ. 1980. Strains patterns in ice cap and implications for strain variations in shear zones. *J. Struct. Geol.* 5: 455–463.

Imbo Y, De Batist M, Canals M, Prieto MJ, Baraza J. 2003. The Gebra slide: A submarine slide on the Trinity Peninsula Margin, Antarctica. *Marine Geology* 193(3-4): 235–252.

Ings SJ, Beaumont C. 2010. Continental margin shale tectonics: Preliminary results from coupled fluid-mechanical models of large-scale delta instability. *Journal of the Geological Society* 167(3): 571–582.

IODP Expedition 340 Scientists. 2012. Lesser Antilles volcanism and landslides: Implications for hazard assessment and long-term magmatic evolution of the arc. IODP Prel. Rept. 340.

Kehle RO. 1970. Analysis of gravity sliding and orogenic translation. *Geological Society of America Bulletin* 81(6): 1641–1664.

Kelfoun K, Druitt T, van Wyk de Vries BVW, Guilbaud MN. 2008. Topographic reflection of the Socompa debris avalanche, Chile. *Bulletin of Volcanology* 70(10): 1169–1187.

Kervyn M, van Wyk de Vries B, Walter TR, Njome MS, Suh CE, Ernst GGJ. 2014. Directional flank spreading at Mount Cameroon volcano: Evidence from analogue modeling. *Journal of Geophysical Research: Solid Earth* 119(10): 7542–7563.

Kligfield R. 1979. The Northern Apennines as a collisional orogen. *American Journal of Science* 279(6): 676–691.

Klinkmüller M, Schreurs G, Rosenau M, Kemnitz H. 2016. Properties of granular analogue model materials: A community wide survey. *Tectonophysics* 684: 23–38.

Knappe E, Manga M, Le Friant A, IODP Expedition 340 Scientists. 2020. Rheology of Natural Sediments and its influence on the settling of dropstones in hemipelagic marine sediment. *Earth and Space Science* 7(3): e2019EA000876.

Koyi H. 1996. Salt flow by aggrading and prograding overburdens. *Geological Society, London, Special Publications* 100(1): 243–258.

Krantz RW. 1991. Measurements of friction coefficients and cohesion for faulting and fault reactivation in laboratory models using sand and sand mixtures. *Tectonophysics* 188(1-2): 203–207.

Lafuerza S, Le Friant A, Manga M, Boudon G, Villemant B, Stroncik N, *et al.* 2014. Geomechanical characterization of submarine volcano-flank sediments, Martinique, Lesser Antilles Arc. In: *Submarine mass movements and their consequences*. Cham: Springer, pp. 73–81.

Le Friant A, Boudon G, Deplus C, Villemant B. 2003a. Large-scale flank collapse events during the activity of Montagne Pelée, Martinique, Lesser Antilles. *Journal of Geophysical Research* 108 (B1): 1–15. https://doi.org/10.1029/2001JB001624.

Le Friant A, Heinrich P, Deplus C, Boudon G. 2003b. Numerical simulation of the last flank-collapse event of Montagne Pelée, Martinique, Lesser Antilles. *Geophys. Res. Lett.* 30(2): 1034.

Le Friant A, Boudon G, Arnulf A, Robertson RE. 2009. Debris avalanche deposits offshore St. Vincent (West Indies): Impact of flank-collapse events on the morphological evolution of the island. *Journal of Volcanology and Geothermal Research* 179 (1): 1–10.

Le Friant A, Ishizuka O, Stroncik NA, IODP Expedition 340 Scientists. 2013. Integrated Ocean Drilling Program Management International, Inc. In: *Proceedings of the Integrated Ocean Drilling Program, Tokyo University of Marine Science and Technology, Tokyo, Japan*. https://doi.org/10.2204/iodp.proc.340.2013.

Le Friant A, Ishizuka O, Boudon G, Palmer MR, Talling PJ, Villemant B, *et al.* 2015. Submarine record of volcanic island construction and collapse in the Lesser Antilles arc: First scientific drilling of submarine volcanic island landslides by IODP Expedition 340. *Geochemistry, Geophysics, Geosystems* 16(2): 420–442.

Lebas E, Le Friant A, Boudon G, Watt SFL, Talling PJ, Feuillet N, *et al.* 2011. Multiple widespread landslides during the long-term evolution of a volcanic island: Insights from high-resolution seismic data, Montserrat, Lesser Antilles. *Geochemistry, Geophysics and Geosystems* 12: Q05006. https://doi.org/10.1029/2010GC003451.

Letouzey J, Colletta B, Vially R, Chermette JC. 1995. Evolution of salt-related structures in compressional settings. *AAPG Memoir* 65: 41–60.

Leynaud D, Sultan N, Mienert J. 2007. The role of sedimentation rate and permeability in the slope stability of the formerly glaciated Norwegian continental margin: The Storegga slide model. *Landslides* 4(4): 297.

Llopart J, Lafuerza S, Le Friant A, Urgeles R, Watremez L. 2021. Long-term and long-distance deformation in submarine volcanoclastic sediments: Coupling of hydrogeology and debris avalanche emplacement off W Martinique Island. *Basin Research* 33(4): 2179–2201.

Locat J, Lee HJ. 2002. Submarine landslides: Advances and challenges. *Canadian Geotechnical Journal* 39: 193–212.

Maloney D, Davies R, Imber J, Higgins S, King S. 2010. New insights into deformation mechanisms in the gravitationally driven Niger Delta deep-water fold and thrust belt. *AAPG Bulletin* 94(9): 1401–1424.

Martin-Kaye PHA. 1969. A summary of the geology of the Lesser Antilles. *Overseas Geology and Mineral Resources* 10(2): 172–206.

Mauduit T, Guerin G, Brun JP, Lecanu H. 1997. Raft tectonics: The effects of basal slope angle and sedimentation rate on progressive extension. *Journal of Structural Geology* 19(9): 1219–1230.

McClay KR, Dooley T, Lewis G. 1998. Analog modeling of progradational delta systems. *Geology* 26(9): 771–774.

McClay K, Dooley T, Zamora G. 2003. Analogue models of delta systems above ductile substrates. *Geological Society, London, Special Publications* 216(1): 411–428.

Mencaroni D, Llopart J, Urgeles R, Lafuerza S, Gràcia E, Le Friant A, *et al.* 2020. From gravity cores to overpressure history: The importance of measured sediment physical properties in hydrogeological models. *Geological Society, London, Special Publications* 500(1): 289–300.

Merle O. 1982. Cinématique et déformation de la nappe du Parpaillon (flysch à Helminthoïdes de l'Embrunais-Ubaye, Alpes occidentales). Thèse de doctorat, Université Rennes 1.

Merle O, Borgia A. 1996. Scaled experiments of volcanic spreading. *Journal of Geophysical Research: Solid Earth* 101(B6): 13805–13817. https://doi.org/10.1029/95JB03736.

Mourgues R, Cobbold PR. 2003. Some tectonic consequences of fluid overpressures and seepage forces as demonstrated by sandbox modelling. *Tectonophysics* 376(1-2): 75–97.

Mourgues R, Lecomte E, Vendeville B, Raillard S. 2009. An experimental investigation of gravity-driven shale tectonics in progradational delta. *Tectonophysics* 474(3): 643–656.

Nalpas T, Györfi I, Guillocheau F, Lafont F, Homewood P. 1999. Influence de la charge sédimentaire sur le développement d'anticlinaux synsédimentaires. Modélisation analogique et exemples de terrain (Bordure sud du bassin de Jaca). *Bulletin de la Société Géologique de France* 170(5): 733–740.

Oehler JF, van Wyk de Vries B, Labazuy P. 2005. Landslides and spreading of oceanic hot-spot and arc shield volcanoes on Low Strength Layers (LSLs): An analogue modeling approach. *Journal of Volcanology and Geothermal Research* 144(1-4): 169–189. https://doi.org/10.1016/j.jvolgeores.2004.11.023.

Osborne MJ, Swarbrick RE. 1997. Mechanisms for generating overpressure in sedimentary basins: A reevaluation. *AAPG Bulletin* 81(6): 1023–1041.

Paguican EMR, van Wyk de Vries BVW, Lagmay AMF. 2014. Hummocks: How they form and how they evolve in rockslide-debris avalanches. *Landslides* 11(1): 67–80.

Price NJ. 1977. Aspect of gravity tectonics and the development of listric faults. *J. Geol. Soc. Lond.* 133: 311–327.

Ramberg H. 1977. Some remarks on the mechanism of nappe movement. *Geologiska Föreningen i Stockholm Förhandlingar* 99 (2): 110–117.

Ramberg H. 1981. Gravity, deformation and the Earth's crust. London: Academic Press.

Rettger RE. 1935. Experiments on soft-rock deformation. *AAPG Bulletin* 19(2): 271–292.

Rouby D, Nalpas T, Jermannaud P, Robin C, Guillocheau F, Raillard S. 2011. Gravity driven deformation controlled by the migration of the delta front: The Plio-Pleistocene of the Eastern Niger Delta. *Tectonophysics* 513(1): 54–67.

Schellart WP. 2000. Shear test results for cohesion and friction coefficients for different granular materials: Scaling implications for their usage in analogue modelling. *Tectonophysics* 324: 1–16.

Shea T, van Wyk de Vries BVW, Pilato M. 2008. Emplacement mechanisms of contrasting debris avalanches at Volcán Mombacho (Nicaragua) provided by structural and facies analysis. *Bulletin of Volcanology* 70(8): 899–921.

Siddans AWB. 1984. Thrust tectonics – A mechanistic view from the West and Central Alps. *Tectonophysics* 104(3): 257–281.

Solaro C, Boudon G, Le Friant A, Balcone-Boissard H, Emmanuel L, Paterne M, *et al.* 2020. New insights into the recent eruptive and collapse history of Montagne Pelée (Lesser Antilles Arc) from offshore marine drilling site U1401A (IODP Expedition 340). *Journal of Volcanology and Geothermal Research* 403: 107001.

Szatmari P, Guerra MCM, Pequeno MA. 1996. Genesis of large counter-regional normal fault by flow of Cretaceous salt in the South Atlantic Santos Basin, Brazil. *Geological Society, London, Special Publications* 100(1): 259–264.

Talbot CJ. 1979. Fold trains in a glacier of salt in southern Iran. *Journal of Structural Geology* 1(1): 5–18.

Talbot CJ. 1981. Sliding and other deformation mechanisms in a glacier of salt, S Iran. *Geological Society, London, Special Publications* 9(1): 173–183.

Trofimovs J, Talling PJ, Fisher JK, Sparks RSJ, Watt SFL, Hart MB, *et al.* 2013. Timing, origin and emplacement dynamics of mass flows offshore of SE Montserrat in the last 110 ka: Implications for landslide and tsunami hazards, eruption history, and volcanic island evolution. *Geochem. Geophys. Geosyst.* 14: 385–406. https://doi.org/10.1002/ggge.20052.

van Wyk de Vries B. 1993. Tectonics and magma evolution of Nicaragua volcanic systems. Unpublished PhD thesis, Department of Earth Sciences, The Open University, UK.

van Wyk de Vries B, Francis PW. 1997. Catastrophic collapse at stratovolcanoes induced by gradual volcano spreading. *Nature* 387 (6631): 387–390.

van Wyk de Vries B, Matela R. 1998. Styles of volcano-induced deformation: Numerical models of substratum flexure, spreading and extrusion. *Journal of Volcanology and Geothermal Research* 81(1): 1–18.

van Wyk de Vries B, Self S, Francis PW, Keszthelyi L. 2001. A gravitational spreading origin for the Socompa debris avalanche. *Journal of Volcanology and Geothermal Research* 105(3): 225–247.

Vendeville B. 1987. Champs de failles et tectonique en extension. Rennes : Université de Rennes 1, 395 p.

Vendeville BC. 2005. Salt tectonics driven by sediment progradation: Part I – Mechanics and kinematics. *AAPG Bulletin* 89(8): 1071–1079.

Vendeville BC, Jackson MPA. 1992. The fall of diapirs during thin-skinned extension. *Marine and Petroleum Geology* 9(4): 354–371.

Vendeville B, Gaullier V. 2003. Role of pore-fluid pressure and slope angle in triggering submarine mass movements: Natural examples and pilot experimental models. In: Locat J, Mienert J, eds. *Submarine mass movements and their consequences*. Dordrecht (Pays-Bas): Kluwer Academic Publishers, pp. 137–144.

Vendeville B, Cobbold P, Davy P, Brun JP, Choukroune P. 1987. Physical models of extensional tectonics at various scales. In: Coward JF, Dewey JF, Hancock PL, eds. *Continental extensional tectonics*. Geological Society of London Special Publications 28, pp. 95–107.

Vliet-Lanoë V. 1995. Solifluxion et transferts illuviaux dans les formations périglaciaires litées. État de la question [Solifluction and translocation processes in bedded periglacial formations. State of the art]. *Géomorphologie : Relief, processus, environnement* 1 (2): 85–113.

von Terzaghi K. 1923. Die Berechnung der Durchassigkeitsziffer des Tones aus dem Verlauf der hydrodynamischen Spannungs. erscheinungen. *Sitzungsber. Akad. Wiss. Math. Naturwiss. Kl. Abt. 2A*, 132: 105–124 (in the text and the “References” section).

Wadge G. 1984. Comparison of volcanic production-rates and subduction rates in the Lesser Antilles and Central America. *Geology* 12(9): 555–558.

Walter TR. 2003. Buttressing and fractional spreading of Tenerife; an experimental approach on the formation of rift zones. *Geophysical Research Letters* 30(6): 1296. https://doi.org/10.1029/2002GL016610.

Walter TR, Troll VR. 2003. Experiments on rift zone evolution in unstable volcanic edifices. *Journal of Volcanology and Geothermal Research* 127(1): 107–120.

Walter TR, Amelung F. 2006. Volcano–earthquake interaction at Mauna Loa volcano, Hawaii. *Journal of Geophysical Research: Solid Earth (1978–2012)* 111(B5).

Watt SFL, Talling PJ, Vardy ME, Heller V, Huehnerbach V, Urlaub M, *et al.* 2012a. Combinations of volcanic-flank and seafloor-sediment failure offshore Montserrat, and their implications for tsunami generation. *Earth and Planetary Science Letters* 319: 228–240. https://doi.org/10.1016/j.epsl.2011.11.032.

Watt SFL, Talling PJ, Vardy ME, Masson DG, Henstock TJ, Huehnerbach TA, *et al.* 2012b. Widespread and progressive seafloor-sediment failure following volcanic debris avalanche emplacement: Landslide dynamics and timing offshore Montserrat, Lesser Antilles. *Marine Geology* 232-325: 69–94. https://doi.org/10.1016/j.margeo.2012.08.002.

Watt SFL, Karstens J, Berndt C. 2021. Volcanic-Island lateral collapses and their submarine deposits. In: Roverato M, Dufresne A, Procter J, eds. *Volcanic debris avalanches. Advances in volcanology (An official book series of the International Association of Volcanology and Chemistry of the Earth's interior)*. Cham: Springer. https://doi.org/10.1007/978-3-030-57411-6_10.

Wise DU. 1963. Keystone faulting and gravity sliding driven by basement uplift of Owl Creek Mountains, Wyoming. *AAPG Bulletin* 47(4): 586–598.

Wu S, Bally AW, Mohriak W, Talwani M. 2000. Slope tectonics-comparisons and contrasts of structural styles of salt and shale tectonics of the northern Gulf of Mexico with shale tectonics of offshore Nigeria in Gulf of Guinea. *Geophysical Monograph-American Geophysical Union* 115: 151–172.

Cite this article as: Brunet M, Nalpas T, Hallot E, Le Friant A, Boudon G, Kermarrec J-J. 2023. Gravity-driven sliding and associated deformations along complex submarine slopes: a laboratory modeling approach based on constraints observed offshore Martinique Island (Lesser Antilles), *BSGF - Earth Sciences Bulletin* 194: 12.